

## Chiral anomalies in three-dimensional spin-orbit coupled metals: Electrical, thermal, and gravitational anomalies

Sunit Das<sup>ⓧ,\*</sup>, Kamal Das<sup>ⓧ,†</sup> and Amit Agarwal<sup>ⓧ,‡</sup>

*Department of Physics, Indian Institute of Technology Kanpur, Kanpur-208016, India*



(Received 25 January 2023; revised 6 May 2023; accepted 8 June 2023; published 10 July 2023)

The discovery of chiral anomaly in Weyl semimetals, the nonconservation of chiral charge and energy across two opposite chirality Weyl nodes, has sparked immense interest in understanding its impact on various physical phenomena. Here, we demonstrate the existence of electrical, thermal, and gravitational quantum chiral anomalies in three-dimensional (3D) spin-orbit coupled systems. Notably, these anomalies involve chiral charge transfer across two Fermi surfaces linked to a single Weyl-type point, rather than across opposite chirality Weyl nodes as in Weyl semimetals. Our findings reveal that the Berry curvature flux piercing the Fermi surface plays a critical role in distinguishing the “chirality” of the carriers and the corresponding chiral charge and energy transfer. Importantly, we demonstrate that these quantum chiral anomalies lead to interesting thermal spin transport such as the spin Nernst effect. Our results suggest that 3D spin-orbit coupled metals offer a promising platform for investigating the interplay between quantum chiral anomalies and charge and spin transport in nonrelativistic systems.

DOI: [10.1103/PhysRevB.108.045405](https://doi.org/10.1103/PhysRevB.108.045405)

### I. INTRODUCTION

Chiral anomaly refers to the nonconservation of chiral charges in the presence of collinear electric and magnetic fields. It was first introduced in the context of the relativistic field theory of chiral fermions [1–3]. Later it was shown to be achievable in low gap semiconductors [4], with signatures in magnetoconductance experiments. Following the discovery of Weyl semimetals (WSMs) in recent years, the physics of chiral anomaly has been widely studied in condensed matter systems, resulting in a variety of nontrivial transport [5–29] and optical [30–41] effects. Intriguingly, the presence of a temperature gradient in Weyl systems can also result in an anomaly similar to the axial-gravitational anomaly in flat-space time [42–45]. This leads to a range of interesting magnetothermal transport phenomena [15,46–53].

Central to the physics of chiral anomaly is the continuity equation for the chiral charge. The continuity equation for the chiral charges and energy can be derived using semiclassical dynamics in crystalline materials and shows that the Berry curvature monopoles govern the chiral anomaly in Weyl metals [54–56]. The concept of chiral anomaly has also been extended to other free-fermionic excitations with no high-energy analog, such as multi-Weyl semimetals [57–62], which exhibit two band crossings similar to WSMs but with nonlinear momentum dispersion along a particular direction, and semimetals with a higher number of band crossings near the Weyl node [63]. These systems, while possessing a higher chiral charge, are otherwise similar to Weyl systems in that a

theory of chiral anomaly requires the presence of two opposite chirality Weyl nodes.

In this paper, we delve into the connection between chiral anomalies and the Berry curvature flux passing through the Fermi surface (FS) [5]. This connection was recently explored in Refs. [64,65]. Motivated by this, we generalize the theory of quantum chiral anomalies to Hamiltonians with nonrelativistic terms, specifically  $\mathbf{H} = \mathbf{h}_k \cdot \boldsymbol{\sigma} + \sigma_0 k^2$ . Here, the  $\boldsymbol{\sigma}$  represents the real spin of the system,  $\sigma_0$  is the identity matrix, and  $\mathbf{h}_k$  is an odd function of  $\mathbf{k}$ . The quadratic kinetic-energy-like term in the Hamiltonian makes the chiral anomaly in these spin-orbit coupled (SOC) metals to be distinctly different from that in WSM (see Fig. 1). These types of systems can be found in Kramers-Weyl metals with quadratic corrections to their  $\mathbf{k} \cdot \mathbf{p}$  Hamiltonians [66–75] or in systems supporting three-dimensional (3D) electron gas with SOC. While some aspects of the charge, heat, and spin transport in SOC metals have been explored earlier [64,76,77], the physics of quantum chiral anomalies in these systems is largely unexplored and merits further investigation.

In this paper, we demonstrate that Kramers-Weyl and spin-orbit coupled metals can exhibit all three types of quantum chiral anomalies: electrical, thermal, and gravitational. We investigate the impact of electric field and temperature-gradient-induced quantum chiral anomalies on charge, heat, and spin transport phenomena. Similar to the behavior observed in Weyl semimetals [24], we find that chiral anomalies in 3D SOC systems also result in negative longitudinal magnetoresistance and positive thermal magnetoresistance. However, a distinct feature of 3D SOC systems, as compared to WSMs, is that their low-energy Hamiltonian involves real spins. We show that quantum chiral anomalies in these systems also lead to interesting electrical and thermal spin transport including the spin Nernst effect.

\*sunitd@iitk.ac.in

†kamaldas@iitk.ac.in

‡amitag@iitk.ac.in

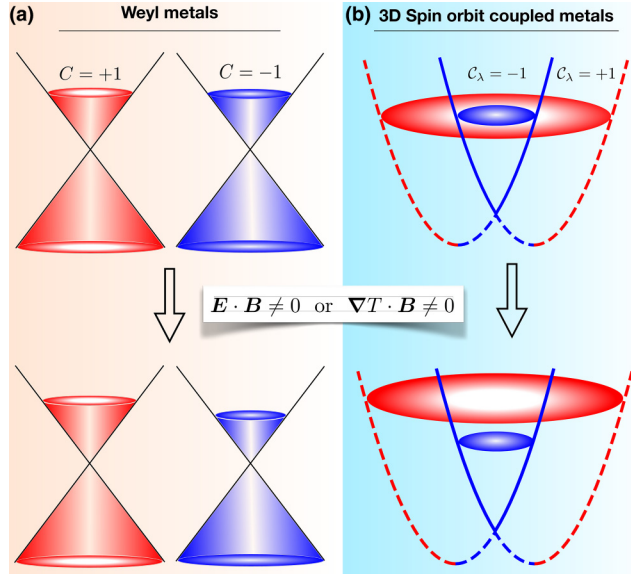


FIG. 1. Depiction of the quantum chiral anomalies in (a) Weyl semimetals and (b) 3D spin-orbit coupled metals or Kramers-Weyl metals. Both systems experience chiral charge and energy pumping, manifesting as electrical, thermal, and gravitational anomalies, when subjected to a magnetic field and collinear electric field ( $\mathbf{E} \cdot \mathbf{B} \neq 0$ ) or a temperature gradient ( $\nabla T \cdot \mathbf{B} \neq 0$ ). In contrast to Weyl semimetals, the chiral charge pumping in 3D spin-orbit coupled metals occurs between two different Fermi surfaces associated with a single “Kramers-Weyl” node, but with opposite Berry curvature flux passing through them.

The structure of the rest of this paper is as follows. In Sec. II, we discuss the origins of chiral anomalies in three-dimensional (3D) metals with SOC and Kramers-Weyl metals. In Sec. III, we present a mathematical derivation of the continuity equations to demonstrate the existence of these anomalies. The effects of these anomalies on charge and spin transport are examined in Secs. IV and V, respectively. Finally, we summarize our findings in Sec. VI.

## II. ORIGIN OF CHIRAL ANOMALIES IN SPIN-ORBIT COUPLED METALS

To understand the chiral anomaly in 3D spin-orbit coupled metallic systems (or Kramers-Weyl metals), we first revisit the WSM. Specifically, we review the physics of chiral anomaly in WSM from the perspective of semiclassical dynamics. In WSM, the Hamiltonian for a particular Weyl node near the band-crossing point can be approximated as  $\mathcal{H}_{\text{WSM}} = \sum_{a=x,y,z} \hbar(\mathbf{v}_a \cdot \mathbf{k})\sigma^a$ , where  $k$  is measured from the Weyl node. The “chirality” of Weyl node is defined as  $C = \text{sign}[\mathbf{v}_x \cdot \mathbf{v}_y \times \mathbf{v}_z]$  [78]. In the semiclassical dynamics picture, the existence of chiral anomaly can be understood by calculating the equilibrium current in the presence of an external magnetic field but no electric field.

The equilibrium charge current for each Weyl node (or the chiral current) arises from the chiral magnetic velocity (see Sec. III A with explicit derivation shown in Appendix C). The chiral current for WSM can be expressed in terms of the Berry curvature flux quantum passing through the FS for the WSM

[24]. This is consistent with the intuitive picture of the Weyl nodes acting as sinks and sources of the Berry curvature. For the pair of Weyl nodes of opposite chirality, their FSs are separated in the momentum space (at least for small energies). In the presence of an external electric field aligned along the magnetic field, the chiral charge carriers are pumped across the FSs with distinct Weyl chirality. This flow is stabilized by internode scattering. This results in different chiral charge densities on the two Weyl nodes [as shown in Fig. 1(a)], and it manifests in several interesting transport phenomena in WSMs [5,24,51]. We emphasize two things here: (i) a minimum of a pair of Weyl nodes of opposite chirality are needed to produce chiral anomaly in WSM, and (ii) the chiral anomaly can be interpreted as an FS phenomenon, where the chiral charges are “pumped” across two FSs enclosing opposite quantum of the Berry curvature flux. These two points will be crucial in investigating the chiral anomalies in Kramers-Weyl metals or 3D SOC metals.

3D SOC metals or Kramers-Weyl metals are structurally chiral crystals with broken inversion symmetry. They host “Weyl”-type nodal points at all the time-reversal-invariant momentum (TRIM) points in their Brillouin zone. While the form of the SOC can be different, a common feature of all such materials is that they have two FSs for each band-crossing point (or the Kramers-Weyl node). This is aided by the kinetic energy term of the form  $\hbar^2 k^2/(2m)$  in their dispersion, which is missing in conventional WSM. We have tabulated all crystalline point groups that support Kramers-Weyl points, along with their low-energy Hamiltonian in the vicinity of the Kramers-Weyl point in Appendix A.

While our discussion applies to all classes of single-crystalline systems of 3D SOC metals or Kramers-Weyl metals listed in Table I, for specific calculations, we consider the Hamiltonian [68,79,80]

$$\mathcal{H} = \frac{\hbar^2 k^2}{2m} \sigma_0 + \alpha \mathbf{k} \cdot \boldsymbol{\sigma}. \quad (1)$$

Here,  $m$  is the effective electron mass,  $\alpha$  is the SOC parameter,  $\boldsymbol{\sigma} = (\sigma_x, \sigma_y, \sigma_z)$  denotes the vector of the Pauli matrices in spin space, and  $\mathbf{k}$  is the Bloch wave vector. We note that in contrast to conventional WSM, the Pauli matrices here denote the physical spins of the itinerant electrons. The energy dispersion for the Hamiltonian in Eq. (1) is

$$\epsilon_\lambda = \frac{\hbar^2 k^2}{2m} + \lambda \alpha k. \quad (2)$$

Here,  $\lambda = \pm 1$  is the spin-split band index which coincides with the eigenvalues of the operator  $\hat{\mathcal{O}} = \hat{\mathbf{k}} \cdot \boldsymbol{\sigma}$ , and  $k = |\mathbf{k}|$ . The corresponding eigenstates are given by  $|u\rangle_+^T = [\cos(\theta_k/2), e^{i\phi_k} \sin(\theta_k/2)]$  and  $|u\rangle_-^T = [\sin(\theta_k/2), -e^{i\phi_k} \cos(\theta_k/2)]$ , with  $\cos \theta_k \equiv k_z/k$  and  $\tan \phi_k \equiv k_y/k_x$ . In Fig. 1(b), the  $\lambda = +1$  ( $\lambda = -1$ ) band is represented by the solid (dashed) line. The two bands of the dispersion relation (2) have a band-touching point (BTP) at  $\epsilon = 0$ . The  $\lambda = +1$  band has a minimum at  $\epsilon = 0$  and increases monotonically as  $k$  increases. The  $\lambda = -1$  band is nonmonotonic, and it has a minimum energy located at  $\epsilon_{\min} = -\epsilon_\alpha$ , with  $\epsilon_\alpha = m\alpha^2/2\hbar^2$ . The minimum energy point lies on a circular contour specified by  $|\mathbf{k}|^2 = k_\alpha^2$ , where  $k_\alpha = m\alpha/\hbar^2$ .

Clearly, there are two different types of FSs for any value of the Fermi energy greater than the energy of the Kramers-Weyl node. For  $\mu > 0$ , the inner and outer Fermi surfaces originate from two different bands, and both of them are interpreted to have electronic characters. In the main text, we focus on the  $\mu > 0$  limit, and the Berry curvature flux quantum through each of the Fermi surfaces is defined as

$$\mathcal{C}_\lambda = \frac{1}{2\pi} \int_{\text{FS}} d\mathbf{S} \cdot \boldsymbol{\Omega}_\lambda. \quad (3)$$

Here,  $d\mathbf{S}$  is the elemental surface area of the FS, and  $\boldsymbol{\Omega}_\lambda$  is the Berry curvature. More interestingly, the flux quantum associated with the FSs is equal and opposite. We explicitly calculate  $\mathcal{C}_\lambda = -\lambda$ . Hence, the Berry curvature flux quantum piercing the outer (inner) FS is  $+1$  ( $-1$ ). See Appendix B for details.

We emphasize that this scenario is distinctively different from the usual WSM with chiral symmetry. In WSM, the pair of FS with the opposite sign of the Berry curvature flux quantum corresponds to two distinct Weyl crossing points separated by momentum or energy. These two Weyl points have opposite chirality, defined by the sign of vector triple product of the velocities around the nodal point. As a result, in the case of WSM, the chirality of charge carriers (denoted by the sign of the Berry curvature flux) and the chirality of the nodal points are intricately related and can be treated as identical. However, in the case of 3D SOC metals, the chirality of the single nodal point and the chirality of the charge carriers are different. In a 3D SOC metal, for  $\mu > 0$ , the two opposite chirality charge carriers reside on distinct inner and outer Fermi surfaces originating from different bands. However, both of them are associated with the same nodal point. The regime when the chemical potential is below the energy of the Kramers-Weyl point is a bit tricky. For  $\mu < 0$ , there is only one Fermi pocket originating from the  $\lambda = -1$  band. However, due to the nonmonotonic band structure of the  $\lambda = -1$  band, the chiral magnetic velocity can be positive or negative in different regions of the Brillouin zone. More interestingly, depending on the sign of the chiral magnetic velocity, the Berry curvature flux contribution of the positive-velocity and negative-velocity regions is positive and negative, respectively. This allows us to define opposite chirality charge carriers within the same Fermi pocket, and this is the basis of the chiral anomaly for  $\mu < 0$ . We present a detailed analysis and calculation for this case in Appendix B.

From the above discussion, it is clear that the ‘‘chirality’’ of the FSs (or the charge carriers) and the band index are not identical. In the main text example for  $\mu > 0$ , the two FS with opposite Berry curvature flux originate from different bands, and the Berry curvature flux for each FS turns out to be  $-\lambda$ . We take advantage of this and use  $\lambda$  as the proxy for FS chirality in the main text for notational simplicity. However, this is generally not true and may not always work [64]. For example, this association does not work in the  $\mu < 0$  limit of the 3D SOC model. Since, for  $\mu < 0$ , both the opposite chirality carriers with opposite Berry curvature flux originate from the  $\lambda = -1$  band, the carriers’ chirality cannot be associated with the band index (see Appendix B).

The nonzero flux associated with the two FSs in SOC metals gives rise to chiral anomalies. This is captured by the

nonconservation of the total flavor charge ( $\mathcal{N}^\lambda$ ) and energy ( $\mathcal{E}^\lambda$ ) in presence of a magnetic field ( $\mathbf{B}$ ) and an electric field ( $\mathbf{E}$ ) or temperature gradient ( $\nabla T$ ). In a clean system of 3D SOC metal, we can obtain

$$\frac{\partial \mathcal{N}^\lambda}{\partial t} \propto -\mathcal{C}_0^\lambda \mathbf{E} \cdot \mathbf{B} \quad \text{and} \quad \frac{\partial \mathcal{N}^\lambda}{\partial t} \propto -\mathcal{C}_1^\lambda \nabla T \cdot \mathbf{B}. \quad (4)$$

A similar calculation for the total energy of each flavor of fermions yields

$$\frac{\partial \mathcal{E}^\lambda}{\partial t} \propto \begin{cases} -(\mu \mathcal{C}_0^\lambda + k_B T \mathcal{C}_1^\lambda) \mathbf{E} \cdot \mathbf{B}, \\ -(\mu \mathcal{C}_1^\lambda + k_B T \mathcal{C}_2^\lambda) \nabla T \cdot \mathbf{B}. \end{cases} \quad (5)$$

Here,  $\mu$  is the chemical potential, and  $k_B T$  is the energy scale of the temperature. The coefficients  $\mathcal{C}_\nu^\lambda$  [Eq. (9)] for  $\nu = \{0, 1, 2\}$  are the coefficients of the electrical, thermal, and gravitational chiral anomalies, respectively. See Sec. III and Eqs. (16) and (17) for more details. More importantly, these are finite only when the Berry curvature flux quantum  $\mathcal{C}_\lambda$  is finite. Thus, the Berry curvature flux quantum plays an important role in defining the particles’ flavor (or chirality) and the associated quantum flavor anomalies (or chiral anomalies). We highlight the chiral charge transfer across the two Fermi surfaces in WSM and in 3D SOC metals, with opposite Berry curvature flux in Fig. 1.

In the next section, we explicitly demonstrate the three chiral anomalies in 3D SOC (or Kramers-Weyl) metals using the idea of equilibrium and nonequilibrium chiral charge and energy currents. We specifically focus on the case when the chemical potential is higher in energy than the Kramers-Weyl point ( $\mu > 0$ ).

### III. CHIRAL CURRENTS AND THE CHIRAL ANOMALIES

In this section, we first show that the existence of equilibrium currents in the presence of a magnetic field hints at the possible existence of chiral anomalies in the system. Next, we explicitly calculate the continuity equation for the chiral charges and energy current in the presence of a magnetic field and either a collinear electric field or a collinear temperature gradient.

#### A. Equilibrium chiral current induced by magnetic field

The equations of motion of charge carriers in the presence of Berry curvature are described by the following semiclassical equation of motion [81,82]:

$$\dot{\mathbf{r}}_\lambda = D_\lambda \left[ \mathbf{v}_\lambda + \frac{e}{\hbar} \mathbf{E} \times \boldsymbol{\Omega}_\lambda + \frac{e}{\hbar} (\mathbf{v}_\lambda \cdot \boldsymbol{\Omega}_\lambda) \mathbf{B} \right], \quad (6a)$$

$$\hbar \dot{\mathbf{k}}_\lambda = D_\lambda \left[ -e\mathbf{E} - e\mathbf{v}_\lambda \times \mathbf{B} - \frac{e^2}{\hbar} (\mathbf{E} \cdot \mathbf{B}) \boldsymbol{\Omega}_\lambda \right]. \quad (6b)$$

Here, ‘‘ $-e$ ’’ is the electronic charge,  $\mathbf{v}_\lambda$  is the band velocity, and  $\boldsymbol{\Omega}_\lambda$  is the Berry curvature. In Eq. (6a),  $D_\lambda \equiv 1/(1 + \frac{e}{\hbar} \boldsymbol{\Omega}_\lambda \cdot \mathbf{B})$  is the phase-space factor, which modifies the invariant phase-space volume according to  $[d\mathbf{k}] \rightarrow [d\mathbf{k}] D_\lambda^{-1}$  [83]. The term  $\frac{e}{\hbar} (\mathbf{v}_\lambda \cdot \boldsymbol{\Omega}_\lambda) \mathbf{B}$  in Eq. (6a) is known as the chiral magnetic velocity and as will see it plays an important role in anomaly-related transport.

For a given FS, the equilibrium chiral charge and energy currents are calculated to be [18]

$$\{J_{e,\text{eq}}^\lambda, J_{\epsilon,\text{eq}}^\lambda\} = \int_{\text{BZ}_\lambda} [dk] \{-e, \epsilon_\lambda\} \frac{e}{\hbar} (\mathbf{v}_\lambda \cdot \boldsymbol{\Omega}_\lambda) f_\lambda. \quad (7)$$

In Eq. (7),  $f_\lambda$  is the equilibrium Fermi distribution function corresponding to the FS  $\lambda$ . We emphasize that the chiral magnetic velocity solely determines the chiral currents, and the band gradient velocity does not contribute to it. Evaluating Eq. (7) for our model Hamiltonian, we obtain general relations for the charge and the energy current [24,33,45]:

$$J_{e,\text{eq}}^\lambda = -e(\mu C_0^\lambda + k_B T C_1^\lambda) \mathbf{B}, \quad (8a)$$

$$J_{\epsilon,\text{eq}}^\lambda = \left( \frac{\mu^2}{2} C_0^\lambda + \mu k_B T C_1^\lambda + \frac{k_B^2 T^2}{2} C_2^\lambda \right) \mathbf{B}. \quad (8b)$$

Here, we note that all the anomaly coefficients appear in the equilibrium current. In Eqs. (8a) and (8b), the coefficients are specified by

$$C_\nu^\lambda = \frac{e}{4\pi^2 \hbar^2} \int d\epsilon \left( \frac{\epsilon - \mu}{k_B T} \right)^\nu \left( -\frac{\partial f_\lambda}{\partial \epsilon_\lambda} \right) C_\lambda. \quad (9)$$

It is evident from Eq. (9) that for any quantum system with finite  $C_\lambda$ , all the chiral anomaly coefficients are nonzero. We mention here that in defining the anomaly coefficients in Eq. (9), we have converted the Fermi-sea integration of Eq. (7) into Fermi-surface integration using the rule of partial derivative. We provide the details of the calculations in Appendix C.

The importance of the equilibrium currents given in Eqs. (8a) and (8b) is multifold. First of all, the presence of finite chiral charges and energy currents in equilibrium is an indication of the existence of chiral anomalies. This is because, for both chiral anomaly and nonzero chiral equilibrium current, nonzero Berry curvature flux is a prerequisite. Second, the chiral charge ( $J_{e,\text{eq}}^+ - J_{e,\text{eq}}^-$ ) and energy ( $J_{\epsilon,\text{eq}}^+ - J_{\epsilon,\text{eq}}^-$ ) currents are nonzero. This highlights that in systems hosting a pair of fermions with opposite Berry curvature flux quantum, the chiral magnetic velocity induces a dissipationless chiral charge and energy current along  $\mathbf{B}$  [15,84–87]. Finally, we can expect a finite anomaly-induced current in nonequilibrium. In equilibrium, the total charge ( $J_{e,\text{eq}}^+ + J_{e,\text{eq}}^-$ ) and energy ( $J_{\epsilon,\text{eq}}^+ + J_{\epsilon,\text{eq}}^-$ ) currents from the two opposite chirality FSs will add up to zero due to same chemical potential and temperature. However, in the presence of chiral chemical potential ( $\mu_+ \neq \mu_-$ ) and chiral temperature ( $T_+ \neq T_-$ ) imbalance induced by the quantum anomalies, these expressions will result in finite charge and energy current.

Note that the general expressions of equilibrium charge and energy currents  $J_{e,\text{eq}}^\lambda$  and  $J_{\epsilon,\text{eq}}^\lambda$  are valid for any 3D systems with band-touching point. These currents originate from the chiral magnetic velocity  $e/\hbar (\mathbf{v}_\lambda \cdot \boldsymbol{\Omega}_\lambda) \mathbf{B}$ . As a result, the equilibrium currents are identically zero for any two-dimensional system, for which  $\mathbf{v}_\lambda \cdot \boldsymbol{\Omega}_\lambda = 0$ . The absence of chiral magnetic velocity in 2D systems forbids the existence of quantum chiral anomalies in two-dimensional systems. For three-dimensional systems,  $\mathbf{v}_\lambda \cdot \boldsymbol{\Omega}_\lambda$  is generally nonzero, which gives rise to finite equilibrium currents. However, to have quantum chiral anomalies in the system, there should be a pair of FS with opposite Berry curvature flux quantum passing through them so that  $J_{e/\epsilon,\text{eq}}^\lambda = -J_{e/\epsilon,\text{eq}}^{-\lambda}$ .

Having discussed the general expressions for the equilibrium charge and energy currents, we now calculate all the anomaly coefficients for a 3D spin-orbit coupled system. For the Hamiltonian in Eq. (1), the Berry curvature is given by  $\boldsymbol{\Omega}_\lambda = -\lambda \mathbf{k}/2k^3$ . The chiral anomaly coefficients are obtained to be

$$\{C_0^\lambda, C_1^\lambda, C_2^\lambda\} = -\lambda \frac{e}{4\pi^2 \hbar^2} \{\mathcal{F}_0, \mathcal{F}_1, \mathcal{F}_2\}. \quad (10)$$

We note that the equilibrium currents of Eqs. (8a) and (8b), along with the chiral anomaly coefficients of the above equations, do not get affected by the orbital magnetic moment. Here,  $\mathcal{F}_\nu$ 's are the dimensionless functions of (i)  $x = \beta(\epsilon_\alpha + \mu)$  for  $\lambda = -1$  band, and (ii)  $x = \beta\mu$  for  $\lambda = +1$  band with  $\beta = 1/k_B T$  being the inverse temperature. Their functional form is given by

$$\mathcal{F}_0(x) \equiv 1/(1 + e^{-x}), \quad (11)$$

$$\mathcal{F}_1(x) \equiv x/(1 + e^x) + \ln[1 + e^{-x}], \quad (12)$$

$$\mathcal{F}_2(x) \equiv \frac{\pi^2}{3} - x \left( \frac{x}{1 + e^x} + 2 \ln[1 + e^{-x}] \right) + 2 \text{Li}_2[-e^{-x}]. \quad (13)$$

Here,  $\text{Li}_2$  is the polylogarithmic function of order two. With the replacement of  $(\epsilon_\alpha + \mu) \rightarrow \mu$ , Eq. (10) and Eqs. (11)–(13) become identical to that in the WSMs [24]. The temperature dependence of all three chiral anomaly coefficients is similar to Fig. 6 in Ref. [24]. In the zero-temperature limit,  $\mathcal{F}_0 \rightarrow 1$  and  $\mathcal{F}_2 \rightarrow \pi^2/3$ . It is worth noting that for  $T = 0$ , the thermal chiral anomaly coefficient  $C_1^\lambda \propto \mathcal{F}_1 \rightarrow 0$  becomes finite only for finite  $T$ .

## B. Steady state in the presence of chiral anomaly

The presence of external perturbations, such as an electric field  $\mathbf{E}$ , or a temperature gradient  $\nabla T$ , drives the system out of equilibrium. In the nonequilibrium steady state, the distribution function ( $g_\lambda$ ) corresponding to the FS  $\lambda$  satisfies the following Boltzmann transport equation:

$$\frac{\partial g_\lambda}{\partial t} + \dot{\mathbf{r}}_\lambda \cdot \nabla_{\mathbf{r}} g_\lambda + \dot{\mathbf{k}}_\lambda \cdot \nabla_{\mathbf{k}} g_\lambda = \mathcal{I}_{\text{coll}}\{g_\lambda\}. \quad (14)$$

Here,  $\mathcal{I}_{\text{coll}}\{g_\lambda\}$  is the collision integral and  $g_\lambda$  is the nonequilibrium distribution function for each Fermi function. Similar to that in WSM, the charge and energy pumping between the two FSs dictates that the collision integral should incorporate both the intra- and inter-Fermi-surface scattering processes [24,51,88]. Within the relaxation time approximation, both the scattering processes can be captured by the following form of the collision integral [16,18]:

$$\mathcal{I}_{\text{coll}}^\lambda = -\frac{g_\lambda - \bar{g}_\lambda}{\tau} - \frac{\bar{g}_\lambda - f_\lambda}{\tau_\nu}. \quad (15)$$

Here,  $\bar{g}_\lambda$  represents the ‘‘local’’ steady-state distribution function for each FS with a local chemical potential  $\mu_\lambda \equiv \mu + \delta\mu_\lambda$ , and local temperature  $T_\lambda \equiv T + \delta T_\lambda$  [88], and  $f_\lambda$  specifies the global equilibrium function. The first term in the right-hand side of Eq. (15) represents the intra-Fermi-surface scattering (with scattering rate  $1/\tau$ ), which establishes the local equilibrium. The inter-Fermi-surface scattering has

been represented by the second term in Eq. (15) with scattering rate  $1/\tau_v$ . The ratio of inter- and intra-Fermi-surface scattering time for Hamiltonian (1) considering screened Coulomb impurity potential has been calculated in Ref. [64]. In the small- $\mu$  limit, it is given by  $\tau_v/\tau \sim (2m\alpha^2/\hbar^2)^2/\mu^2$  [64]. Hence, for small  $\mu$ , similar to the WSM [7,89], we have  $\tau_v > \tau$ .

Now, we construct the continuity equation for the particle number and the energy density. Substituting Eq. (15) in (14), and then integrating over all the momentum states for the FS  $\lambda$ , we obtain

$$\frac{\partial \mathcal{N}^\lambda}{\partial t} + e\mathbf{E} \cdot \mathbf{B}C_0^\lambda + \nabla_{\mathbf{r}} \cdot \mathbf{J}_e^\lambda = -\frac{\mathcal{N}^\lambda - \mathcal{N}_0^\lambda}{\tau_v}. \quad (16)$$

Here,  $\nabla_{\mathbf{r}} \cdot \mathbf{J}_e^\lambda = k_B C_1^\lambda \nabla T \cdot \mathbf{B}$  is the divergence of particle current. The quantities  $\{\mathcal{N}_0^\lambda, \mathcal{N}^\lambda\} = \int [d\mathbf{k}] D_\lambda^{-1} \{f_\lambda, g_\lambda\}$  represent the total particle number density in each FS before and after applying the perturbing fields. In Eq. (16), the terms  $\mathbf{E} \cdot \mathbf{B}C_0^\lambda$ , and  $k_B C_1^\lambda \nabla T \cdot \mathbf{B}$  represent the chiral-anomaly-induced flow of the charge carriers. Similarly, the continuity equation for the energy density, which we construct by multiplying the energy dispersion  $\epsilon_\lambda$  in Eq. (14) and integrating over all the momentum states, is obtained to be

$$\frac{\partial \mathcal{E}^\lambda}{\partial t} + (\mu C_0^\lambda + k_B T C_1^\lambda) e\mathbf{E} \cdot \mathbf{B} + \nabla_{\mathbf{r}} \cdot \mathbf{J}_\mathcal{E}^\lambda = -\frac{\mathcal{E}^\lambda - \mathcal{E}_0^\lambda}{\tau_v}. \quad (17)$$

The second term on the left-hand side is  $-\mathbf{E} \cdot \mathbf{j}_{e,\text{eq}}^\lambda$  that represents the work performed by the electric field and  $\nabla_{\mathbf{r}} \cdot \mathbf{J}_\mathcal{E}^\lambda = (\mu k_B C_1^\lambda + k_B^2 T C_2^\lambda) \nabla T \cdot \mathbf{B}$  represents the divergence of energy current in presence of  $\nabla T$ . The quantities  $\{\mathcal{E}_0^\lambda, \mathcal{E}^\lambda\} = \int [d\mathbf{k}] D_\lambda^{-1} \epsilon_\lambda \{f_\lambda, g_\lambda\}$  are the total energy density in each FS before and after applying external fields, respectively. Here,  $\mu C_0^\lambda$  and  $\mu C_1^\lambda$  specify the energy carried out by the chiral charge transfer, whereas  $T C_2^\lambda$  represents the energy pumped out by the term  $\nabla T \cdot \mathbf{B}$  [24]. In constructing Eqs. (16) and (17), we have used the fact that the intra-Fermi-surface scattering does not change the number of particles and energy in each FS. The detailed derivation of Eqs. (16) and (17) is outlined in Appendix D.

#### IV. CHIRAL ANOMALY AND CARRIER TRANSPORT

To calculate the chiral-anomaly-induced charge, heat, and spin currents, we first calculate the nonequilibrium distribution function to linear order in applied perturbing field. In the linear response regime, we can safely assume that the change in chiral chemical potential and temperature is small, i.e.,  $\delta\mu_\lambda < \mu$ , and  $\delta T_\lambda < T$  [18,24,88]. Then, to the lowest order in  $\delta\mu_\lambda$  and  $\delta T_\lambda$ , the nonequilibrium distribution function can be calculated to be

$$g_\lambda = f_\lambda + \left( -\frac{\partial f_\lambda}{\partial \epsilon_\lambda} \right) \left[ \left( 1 - \frac{\tau}{\tau_v} \right) \left( \delta\mu_\lambda + \frac{\epsilon_\lambda - \mu}{T} \delta T_\lambda \right) - \tau D_\lambda \left( \mathbf{v}_\lambda + \frac{e}{\hbar} (\mathbf{v}_\lambda \cdot \boldsymbol{\Omega}_\lambda) \mathbf{B} \right) \cdot \left( e\mathbf{E} + (\epsilon_\lambda - \mu) \frac{\nabla T}{T} \right) \right]. \quad (18)$$

Here, the chiral chemical potentials  $\delta\mu_\lambda$  and temperature  $\delta T_\lambda$  are given by [18]

$$\delta\mu_\lambda = -\frac{\tau_v}{(\mathcal{D}_2^\lambda \mathcal{D}_0^\lambda - \mathcal{D}_1^\lambda)^2} \left[ (\mathcal{D}_2^\lambda C_0^\lambda - \mathcal{D}_1^\lambda C_1^\lambda) e\mathbf{E} \cdot \mathbf{B} + (\mathcal{D}_2^\lambda C_1^\lambda - \mathcal{D}_1^\lambda C_2^\lambda) k_B \nabla T \cdot \mathbf{B} \right], \quad (19)$$

$$k_B \delta T_\lambda = -\frac{\tau_v}{(\mathcal{D}_2^\lambda \mathcal{D}_0^\lambda - \mathcal{D}_1^\lambda)^2} \left[ (\mathcal{D}_0^\lambda C_1^\lambda - \mathcal{D}_1^\lambda C_0^\lambda) e\mathbf{E} \cdot \mathbf{B} + (\mathcal{D}_0^\lambda C_2^\lambda - \mathcal{D}_1^\lambda C_1^\lambda) k_B \nabla T \cdot \mathbf{B} \right]. \quad (20)$$

In the above equation, we have defined the magnetic-field-dependent generalized density of states at finite temperature as

$$\mathcal{D}_\nu^\lambda = \int d\epsilon \left( \frac{\epsilon_\lambda - \mu}{k_B T} \right)^\nu \left( -\frac{\partial f_\lambda}{\partial \epsilon_\lambda} \right) \mathcal{D}_\lambda. \quad (21)$$

Here,  $\nu = \{0, 1, 2\}$ , and  $\mathcal{D}_\lambda = \int [d\mathbf{k}] (1 + e/\hbar \boldsymbol{\Omega}_\lambda \cdot \mathbf{B}) \delta(\mu - \epsilon_\lambda)$  being the density of states corresponding to the FS of the band  $\lambda$ . It is evident that both the electric field and the temperature gradient components parallel to  $\mathbf{B}$  contribute to generating the system's chiral chemical potential and chiral temperature imbalance.

Having obtained the nonequilibrium distribution function, we now calculate the charge and heat current in each FS, which are defined as  $\{\mathbf{j}_e^\lambda, \mathbf{j}_Q^\lambda\} = \int [d\mathbf{k}] \{-e, (\epsilon_\lambda - \mu)\} \mathbf{r}_\lambda g_\lambda$ . Focusing only on the anomaly-induced contribution  $\propto \tau_v$ , we obtain [18]

$$\begin{pmatrix} \mathbf{j}_e^\lambda \\ \mathbf{j}_Q^\lambda \end{pmatrix} = \tau_v \mathbf{B} \begin{pmatrix} \frac{1}{\mathcal{D}_0^\lambda} (eC_0^\lambda)^2 & e k_B \frac{\mathcal{D}_1^\lambda}{\mathcal{D}_0^\lambda \mathcal{D}_2^\lambda} C_0^\lambda C_2^\lambda \\ e k_B T \frac{\mathcal{D}_1^\lambda}{\mathcal{D}_0^\lambda \mathcal{D}_2^\lambda} C_0^\lambda C_2^\lambda & T \frac{1}{\mathcal{D}_2^\lambda} (k_B C_2^\lambda)^2 \end{pmatrix} \times \begin{pmatrix} \mathbf{E} \cdot \mathbf{B} \\ -\nabla T \cdot \mathbf{B} \end{pmatrix}. \quad (22)$$

In deriving the above equation, we used the fact that in the  $\mu \gg k_B T$  limit (or  $\beta\mu \gg 1$ ) limit,  $C_1^\lambda \rightarrow 0$ , and  $\mathcal{D}_0^\lambda, \mathcal{D}_2^\lambda > \mathcal{D}_1^\lambda$ . Now, the transport coefficients can be obtained by comparing the total currents ( $\mathbf{j}_{e,Q} = \sum_\lambda \mathbf{j}_{e,Q}^\lambda$ ) from Eq. (22) and the phenomenological linear response relations [90]  $\mathbf{j}_{e,a} = \sum_b [\sigma_{ab} E_b - \alpha_{ab} \nabla_b T]$  and  $\mathbf{j}_{Q,a} = \sum_b [\bar{\alpha}_{ab} E_b - \bar{\kappa}_{ab} \nabla_b T]$ . Here,  $\sigma$ ,  $\alpha$ ,  $\bar{\alpha}$ , and  $\bar{\kappa}$  denote the electrical, thermoelectric, electrothermal, and constant voltage thermal conductivity matrix, respectively. Note that the thermopower matrix is defined as  $S_{ab} = [\sigma^{-1} \alpha]_{ab}$ , and the open circuit thermal conductivity matrix is expressed as  $\kappa_{ab} = [\bar{\kappa} - \bar{\alpha} \sigma^{-1} \alpha]_{ab}$ . From Eq. (22), we see that both the charge and energy currents flow along the direction of the magnetic field. This is consistent with the fact that these originate from the chiral magnetic velocity.

We calculate the generalized energy density using the Sommerfeld approximation in the limit  $\mu \gg k_B T$ . Retaining only the leading-order term in the Sommerfeld expansion, we obtain

$$\mathcal{D}_\nu^\lambda \approx \frac{m^{3/2} \sqrt{\epsilon_\alpha}}{\sqrt{2\pi^2 \hbar^3}} \begin{cases} \frac{(1+\lambda\sqrt{1+\tilde{\mu}})^2}{\sqrt{1+\tilde{\mu}}} \mathcal{F}_0 & \nu = 0, \\ \frac{\tilde{\mu}}{2\beta\epsilon_\alpha(1+\tilde{\mu})^{3/2}} \mathcal{F}_2 & \nu = 1, \\ \frac{(1+\lambda\sqrt{1+\tilde{\mu}})^2}{\sqrt{1+\tilde{\mu}}} \mathcal{F}_2 & \nu = 2. \end{cases} \quad (23)$$

Here, we have defined the scaled chemical potential  $\tilde{\mu} = \mu/\epsilon_\alpha$ . In calculating the above-generalized energy densities,

we have neglected the magnetic field corrections, which are very small. Note that (i)  $\mathcal{D}_0^\lambda$  becomes the exact density of states in the zero-temperature limit for the corresponding bands [91], and (ii)  $\mathcal{D}_1^\lambda$  is independent of  $\lambda$ , i.e., it is identical for both the FSs.

The chiral-anomaly-induced transport coefficients ( $\sigma$ ,  $\alpha$ ,  $\bar{\alpha}$ , and  $\bar{\kappa}$ ) is obtained from Eq. (22) using the expressions of  $\mathcal{C}_v^\lambda$ , and  $\mathcal{D}_v^\lambda$ . In the  $\mu \gg k_B T$  limit, for arbitrary orientation of the magnetic field, the anomalies-induced transport coefficients are

$$\begin{pmatrix} \sigma_{ab} & \alpha_{ab} \\ \bar{\alpha}_{ab} & \bar{\kappa}_{ab} \end{pmatrix} = \frac{\tau_v e^3 B^2}{4\pi^2 m^2 \alpha \tilde{\mu}^2} \mathcal{A}_{ab}(\theta, \phi) \begin{pmatrix} e\sqrt{1+\tilde{\mu}}(2+\tilde{\mu}) & \frac{\pi^2 k_B}{6\beta\epsilon_\alpha} \frac{(\tilde{\mu}^2+8(1+\tilde{\mu}))}{\tilde{\mu}\sqrt{1+\tilde{\mu}}} \\ \frac{\pi^2}{6\beta^2\epsilon_\alpha} \frac{(\tilde{\mu}^2+8(1+\tilde{\mu}))}{\tilde{\mu}\sqrt{1+\tilde{\mu}}} & \frac{\pi^2 k_B}{3e\beta} \sqrt{1+\tilde{\mu}}(2+\tilde{\mu}) \end{pmatrix}. \quad (24)$$

Here,  $\mathcal{A}(\theta, \phi)$  is a  $3 \times 3$  matrix, which captures the angular dependence of all the transport coefficients, with  $(\theta, \phi)$  denoting the polar and azimuthal angle of the spherical polar coordinate for the magnetic field. The  $\mathcal{A}(\theta, \phi)$  matrix is obtained to be

$$\mathcal{A}(\theta, \phi) = \begin{pmatrix} \sin^2 \theta \cos^2 \phi & \frac{1}{2} \sin^2 \theta \sin 2\phi & \frac{1}{2} \sin 2\theta \cos \phi \\ \frac{1}{2} \sin^2 \theta \sin 2\phi & \sin^2 \theta \sin^2 \phi & \frac{1}{2} \sin 2\theta \sin \phi \\ \frac{1}{2} \sin 2\theta \cos \phi & \frac{1}{2} \sin 2\theta \sin \phi & \cos^2 \theta \end{pmatrix}. \quad (25)$$

As a consistency check, we note that the longitudinal electrical conductivity ( $\sigma_{aa}$ ) derived above matches with that obtained recently in Ref. [64]. The conductivity matrix of Eq. (24) is valid for the arbitrary direction of the applied magnetic field. So, in the planar configuration of the magnetic field ( $\theta = \pi/2$ ), the  $xy$  component of the transport coefficients represents various planar Hall effects. For instance, the  $\sigma_{xy}$ ,  $\alpha_{xy}$ ,  $\bar{\alpha}_{xy}$ , and  $\bar{\kappa}_{xy}$  represent the usual planar Hall response, planar Nernst effect, planar Ettinghausen effect, and planar Righi-Leduc effects, respectively [90]. Hence, our work generalizes the chiral-anomalies-induced transport to the thermoelectric and thermal conductivity matrices for spin-orbit coupled systems. We emphasize that the chiral-anomaly-induced responses of Eq. (24) become zero for  $\epsilon_\alpha = 0$ . This is expected because the system's inversion symmetry is restored as  $\alpha \rightarrow 0$ , causing the ‘‘Weyl’’ point, related Berry curvature, and chiral magnetic velocity to vanish.

We present the variation of chiral-anomaly-induced electrical conductivity with  $\mu$  and  $\epsilon_\alpha$  in Fig. 2. We find that the other conductivity components of Eq. (24) also follow a similar qualitative trend in  $\mu$  and  $\alpha$ . The anomaly-induced response decreases as  $\mu$  increases. This is consistent with the fact that the chiral anomalies originate from the Berry curvature, which peaks in the vicinity of the band-touching points.

To investigate the impact of the chiral anomaly on various longitudinal transport phenomena, we define the following generalized magnetoresistance:  $\text{MR}_{\mathcal{R}} \equiv \mathcal{R}(B)/\mathcal{R}(B=0) - 1$ . Here,  $\mathcal{R}$  denotes the different transport contributions in Eq. (24). In the  $\mu \gg k_B T$  limit, we calculate the Drude conductivities to be

$$\sigma_D = \frac{\epsilon\tau m\alpha}{3\hbar^4} \times \frac{2e\epsilon_\alpha}{\pi^2} (2+\tilde{\mu})\sqrt{1+\tilde{\mu}}, \quad (26)$$

$$\alpha_D = -\frac{\epsilon\tau m\alpha}{3\hbar^4} \times \frac{k_B}{3\beta} \frac{(3\tilde{\mu}+4)}{\sqrt{1+\tilde{\mu}}}, \quad (27)$$

$$\bar{\kappa}_D = \frac{\epsilon\tau m\alpha}{3\hbar^4} \times \frac{2\epsilon_\alpha}{e\pi^2} \frac{\pi^2 k_B}{3\beta} (2+\tilde{\mu})\sqrt{1+\tilde{\mu}}. \quad (28)$$

In this limit, the longitudinal MR in resistivity is obtained to be

$$\text{MR}_\rho = -\frac{3\tau_v\gamma^2}{3\tau_v\gamma^2 + 4\tau}. \quad (29)$$

Here we have defined  $\gamma = \frac{e\hbar^3 B}{m^2 \alpha^2 \tilde{\mu}}$ . The ‘‘magnetoresistance’’ in the Seebeck coefficient can be calculated to be

$$\text{MR}_S = \text{MR}_\rho \frac{4(\tilde{\mu}^2 + 3\tilde{\mu} + 2)}{\tilde{\mu}(3\tilde{\mu} + 4)}. \quad (30)$$

We note that both of these,  $\text{MR}_\rho$  and  $\text{MR}_S$ , show negative magnetoresistance, similar to the band-inversion WSM [24]. However, unlike the case of conventional WSM, the relation  $\text{MR}_\rho/\text{MR}_S = \frac{1}{2}$  is not satisfied in spin-orbit coupled systems.

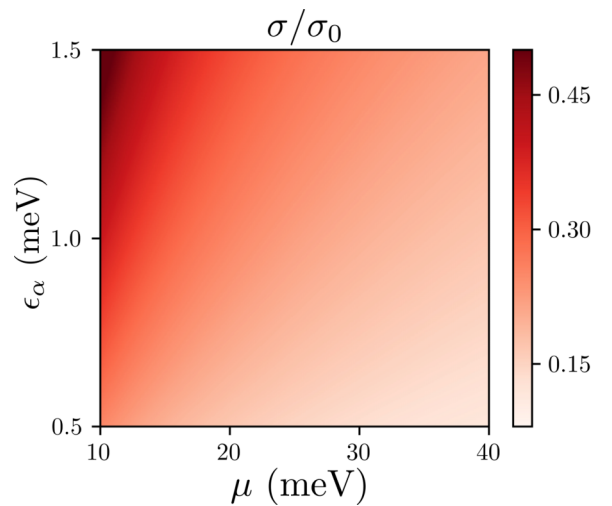


FIG. 2. Variation of the chiral-anomaly-induced electrical conductivity with the chemical potential and the spin-orbit coupling strength. The electrical conductivity is expressed in units of  $\sigma_0 = \frac{\tau_v e^4 B^2}{4\sqrt{2}\pi^2 m^3/2\hbar}$ . The anomaly-induced response is larger for larger SOC strength and smaller chemical potential. Here, we have used  $\alpha = 0.7 \text{ eV \AA}$ , and  $m = 1.4m_e$ , where  $m_e$  is the electronic mass [68].

In the case of constant voltage thermal conductivity and thermoelectric conductivity, we find

$$\text{MR}_{\bar{k}} = \frac{3\tau_v}{4\tau} \gamma^2, \quad (31)$$

$$\text{MR}_{\alpha} = -\text{MR}_{\bar{k}} \frac{\tilde{\mu}^2 + 8(1 + \tilde{\mu})}{\tilde{\mu} \sqrt{1 + \tilde{\mu}} (3\tilde{\mu} + 4)}. \quad (32)$$

Clearly,  $\text{MR}_{\alpha}$  is negative while  $\text{MR}_{\bar{k}}$  is positive. This is similar to the results obtained for WSM in Refs. [24,92].

## V. CHIRAL ANOMALY AND SPIN TRANSPORT

Unlike WSM, where the Pauli matrices in the Hamiltonian represent pseudospins, the Pauli matrices in SOC systems described by Eq. (1) represent physical spins. Consequently, the two bands in SOC systems are spin momentum locked with opposite spin orientations on the inner and outer FSs [93]. Thus, it is natural to expect that chiral anomalies can also influence spin transport [94] along with charge transport. Motivated by this, we explore the chiral-anomalies-induced linear spin transport ( $\propto \mathbf{E} \cdot \mathbf{B}$  or  $\nabla T \cdot \mathbf{B}$ ) in this section. Spin transport in a 3D SOC system was recently explored in Ref. [93] without considering the effect of chiral anomaly. In Ref. [64], the authors studied electrical chiral-anomaly-induced linear electrical spin current in 3D SOC systems. Here, we include the temperature-gradient-induced spin currents and study the chiral-anomaly-induced spin Nernst effect, in addition to other effects.

The spin current operator is defined via the anticommutator relation  $\hat{J}_a^{sb} = \frac{1}{2} \{ \hat{v}_a, \hat{s}_b \}$ , where  $\hat{v}_a$  is the velocity operator,  $\hat{s}_b$  is the spin operator, and  $a, b$  denote the Cartesian coordinates [95]. Now, the spin current can be calculated as the expectation value of the spin current operator weighted by the nonequilibrium distribution function

$$j_a^{sb} = \sum_{\lambda} \int [dk] D_{\lambda}^{-1} \langle u_{\lambda}(\mathbf{k}) | \hat{J}_a^{sb} | u_{\lambda}(\mathbf{k}) \rangle g_{\lambda}. \quad (33)$$

The matrix of spin transport coefficients is related to the spin current via the relation  $j_a^{sb} = \sigma_{ac}^{sb} E_c - \alpha_{ac}^{sb} \nabla_c T$ . Here,  $\sigma_{ac}^{sb}$  is the electrical spin conductivity matrix, and  $\alpha_{ac}^{sb}$  is the thermoelectric spin conductivity matrix. These tensors represent response coefficients for the spin current flowing along the  $a$  direction for spin polarization along the  $b$  direction, while the electric field or the temperature gradient is applied along the  $c$  direction.

The spin current operator for Hamiltonian (1) is given by

$$\hat{J}_a^{sb} = \frac{\hbar k_a}{m} \sigma_0 + \delta_{ab} \frac{\alpha}{\hbar} \sigma_b, \quad (34)$$

where  $\delta_{ab} = 0$  or 1 depending on  $a \neq b$  or  $a = b$ , respectively. Using the eigenstates of Hamiltonian (1), we evaluate the expectation value of the above equation to be

$$\langle u_{\lambda} | \hat{J}_a^{sb} | u_{\lambda} \rangle = \frac{\alpha}{\hbar} \mathbb{I}_{ab} + \lambda \frac{\hbar k}{m} \mathcal{A}_{ab}(\theta_k, \phi_k). \quad (35)$$

Here,  $\mathbb{I}$  denotes the  $3 \times 3$  identity matrix, and  $\mathcal{A}(\theta_k, \phi_k)$  is a  $3 \times 3$  matrix defined in Eq. (25). Following the symmetric energy dispersion, the distribution function  $g_{\lambda}$  [see Eq. (18)] is independent of  $\theta_k$  and  $\phi_k$ . As a consequence, the angular integration over  $\phi_k$  makes all the off-diagonal elements of  $\langle u_{\lambda} | \hat{J}_a^{sb} | u_{\lambda} \rangle$  to be zero, and  $j_a^{sb} = 0$  for  $a \neq b$ . Thus, the spin

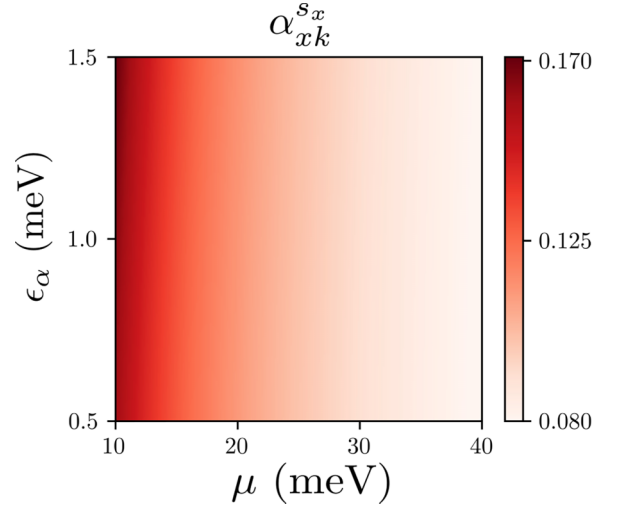


FIG. 3. The variation of the longitudinal thermoelectric spin conductivity with the chemical potential  $\mu$  and the spin-orbit coupling energy strength  $\epsilon_{\alpha}$ . The conductivity  $\alpha_{xk}^{sx}$  is scaled by  $\frac{\tau_v e^2 k_B B}{9\sqrt{2} \hbar^2 \beta \sqrt{m}}$ . Similar to the chiral-anomaly-induced electrical response, the chiral-anomaly-induced spin response is also larger for larger spin-orbit coupling and smaller chemical potential. The parameters used in this plot are identical to those in Fig. 2.

current is finite only when the spins are aligned along the direction of the velocity of the carriers. Hence, the chiral-anomaly-induced spin currents are finite only when the spins are polarized along the respective directions of current, and we have  $j_x^{sx} = j_y^{sy} = j_z^{sz} = j_{CA}^s$ . We calculate the spin current induced by the chiral anomalies to be (see Appendix E for details)

$$j_{CA}^s = \tau_v \sum_{\lambda} \frac{C_0^{\lambda}}{D_0^{\lambda}} \left[ \frac{D_1^{\lambda}}{D_2^{\lambda}} \mathcal{L}_1 - \mathcal{L}_0 \right] e \mathbf{E} \cdot \mathbf{B} - \frac{C_2^{\lambda}}{D_2^{\lambda}} \left[ \frac{D_1^{\lambda}}{D_0^{\lambda}} \mathcal{L}_0 - \mathcal{L}_1 \right] k_B \nabla T \cdot \mathbf{B}. \quad (36)$$

Here, we have defined

$$\mathcal{L}_v = \int [dk] \left( \frac{\alpha}{\hbar} + \lambda \frac{\hbar}{m} \mathbf{k}_a \cdot \hat{\mathbf{k}} \right) \left( \frac{\epsilon_{\lambda} - \mu}{k_B T} \right)^v \left( -\frac{\partial f_{\lambda}}{\partial \epsilon_{\lambda}} \right), \quad (37)$$

with  $\mathbf{k}_a = k_a \hat{\mathbf{a}}$  being a vector along the  $a$  direction with magnitude equal to the component of  $\mathbf{k}$  along the  $a$  direction, and  $\hat{\mathbf{k}} = \sin \theta_k \cos \phi_k \hat{\mathbf{x}} + \sin \theta_k \sin \phi_k \hat{\mathbf{y}} + \cos \theta_k \hat{\mathbf{z}}$ . We now have  $j_a^{sa} \propto \mathbf{E} \cdot \mathbf{B}$  for any arbitrary direction of the applied electric field along the  $k$  direction. We calculate the corresponding chiral-anomaly-induced electrical spin conductivity to be

$$\sigma_{xc}^{sx} = \sigma_0^s \left[ \sqrt{1 + \tilde{\mu}} - \frac{\pi^2}{6\beta^2 \epsilon_{\alpha}^2} \frac{(\tilde{\mu}^2 + 9\tilde{\mu} - 20)}{\tilde{\mu}^2 (1 + \tilde{\mu})^2} \right] \hat{\mathbf{c}} \cdot \hat{\mathbf{B}}, \quad (38)$$

where we have defined  $\sigma_0^s = \frac{\tau_v e^2 B \alpha}{6\pi^2 \hbar^3}$ . The second term on the right-hand side of Eq. (38) is the finite-temperature correction to the electrical spin conductivity, which vanishes in the  $T \rightarrow 0$  limit.

For the thermoelectric part of the spin conductivity, we find that it behaves like the electric spin conductivity. All the thermoelectric spin currents, where the spin is not aligned along the current direction, vanish. We obtain  $j_a^{sb} = 0$ , for

$b \neq a$ , and  $j_a^{s_a} \propto \nabla T \cdot \mathbf{B}$ . Our calculations show that only the conductivity components  $\alpha_{ac}^{s_a}$  are finite, and  $\alpha_{xc}^{s_x} = \alpha_{yc}^{s_y} = \alpha_{zc}^{s_z}$ . We calculate the thermoelectric spin conductivity for the temperature gradient applied along the  $c$  direction to be

$$\alpha_{xc}^{s_x} = \alpha_0^s \left[ \frac{2}{\tilde{\mu}^2} + \frac{\tilde{\mu}^2 + 3\tilde{\mu} - 2}{\tilde{\mu}^2 \sqrt{1 + \tilde{\mu}}} - \frac{\tilde{\mu}^2 + 7\tilde{\mu} + 6}{2\tilde{\mu}(1 + \tilde{\mu})^{3/2}} \right] \hat{c} \cdot \hat{\mathbf{B}}, \quad (39)$$

where  $\alpha_0^s = \frac{\tau_0 e k_B \alpha B}{18 \hbar^3 \beta \epsilon_\alpha}$ . The above expression represents the chiral-anomaly-induced spin-Seebeck (for  $c = x$ ) or the spin Nernst coefficient (for  $c \neq x$ ), with the spins polarized along the  $x$  direction. The variation of  $\alpha_{xc}^{s_x}$  with  $\mu$  and  $\epsilon_\alpha$  is presented in Fig. 3. The electrical spin conductivity also follows similar trends in  $\mu$  and  $\epsilon_\alpha$ . The anomaly-induced effects in general decrease with increasing  $\mu$  and increase with increasing  $\alpha$  which is a proxy for the degree of inversion symmetry breaking.

## VI. CONCLUSION

In summary, we have provided evidence that quantum chiral anomalies can be understood as a feature of FSs. Specifically, the chirality of charge carriers can be determined by the sign of the Berry curvature quantum passing through the associated Fermi surface. This has significant implications for 3D SOC metals or Kramers-Weyl metals, where chiral charge pumping can occur across the two Fermi surfaces associated with a single Kramers-Weyl node. To the best of our knowledge, this kind of chiral anomaly has no analog in relativistic field theories of chiral fermions. We have also demonstrated the existence of three distinct types of quantum chiral anomalies (electrical, thermal, and gravitational) in 3D SOC metals and Kramers-Weyl metals.

The effect of these quantum chiral anomalies can be observed in electrical and thermoelectric charge and spin transport in 3D SOC metals and Kramers-Weyl metals. While the electrical transport signatures of chiral anomalies in 3D spin-orbit coupled metals are similar to those in Weyl semimetals, the signatures in electrical and thermoelectric spin transport are unique to 3D SOC metals. We have shown that spin conductivities are finite only when spins are polarized along the direction of carrier flow. We found that the chiral-anomaly-induced spin conductivities are proportional to the strength of the magnetic field, unlike charge conductivities which scale with the square of the magnetic field. Our findings contribute to the understanding of chiral-anomaly-induced charge, heat, and spin transport in 3D SOC metals and Kramers-Weyl systems.

## ACKNOWLEDGMENTS

We acknowledge the Science and Engineering Research Board (SERB, via Project No. MTR/2019/001520) for financial support. S.D. thanks the MHRD, India, for funding through the Prime Minister's Research Fellowship (PMRF). We sincerely thank A. Chakraborty for the useful discussions.

## APPENDIX A: 3D NONCENTROSYMMETRIC SOC METALS AND KRAMERS-WEYL METALS

In this Appendix, we discuss the SOC-induced chiral anomaly in other 3D systems with different forms of the SOC,

compared to Eq. (1). Comparing the list of single-crystalline point groups which support 3D spin-orbit coupled metals [96] with the list of Kramers Weyl metals [67], we find that these are identical. However, 3D electron gas with SOC can also arise in some heterostructures of two different single crystals. Both of these systems have doubly degenerate band-touching points, which we refer to as ‘‘Kramers-Weyl’’ points. Kramers-Weyl metals are realized in structurally chiral crystals that lack mirror, inversion, or rotoinversion symmetry [67]. There are 65 Sohncke chiral space groups corresponding to 11 chiral point groups which characterize the structurally chiral crystals [70].

The bands of nonmagnetic chiral crystals are at least doubly degenerate at the time-reversal-invariant momenta (TRIM) points due to Kramers theorem [67]. However, the SOC lifts the Kramer's degeneracy at all other points in the momentum space, leaving behind Weyl-type Kramers-Weyl nodes at the TRIM points. All these band-degenerate points are topologically nontrivial, carrying finite Chern numbers [67]. In general, the chiral crystals can host multiple band crossings at the TRIM points in the Brillouin zone along with multifold band degeneracy [66–68,70,74].

In this paper, we focus on Kramers-Weyl metals that have a twofold-degenerate Kramers-Weyl point at TRIM. In Table I, we summarize the chiral space groups and point groups which support Kramers-Weyl fermions, along with some material examples [64,67,96,97]. The generic Kramers-Weyl system will have a low-energy Hamiltonian of the form  $\mathcal{H} = \sum_{ab} \hbar^2 k_a k_b / (2m_{ab}) + \mathbf{h}_k \cdot \boldsymbol{\sigma}$ , in the vicinity of the Kramers-Weyl point for which  $|\mathbf{h}_k| = 0$ . Here,  $a, b = x, y, z$ ,  $m_{ab}$  is the effective mass tensor, and  $\mathbf{k}$  is the momentum with respect to the Kramers-Weyl point. The specific form of symmetry allowed  $\mathbf{h}_k$  for each of the chiral point groups is also summarized in Table I. Each of these Kramers-Weyl points has a chiral charge with value  $\pm 1$ . For example, the Hamiltonian (1) with isotropic SOC term  $\alpha \mathbf{k} \cdot \boldsymbol{\sigma}$  can be realized in point groups **T** and **O** in  $\text{K}_2\text{Sn}_2\text{O}_3$ ,  $\beta$ -RhSi, CoSi crystals [67,68,72–75].

## APPENDIX B: BERRY CURVATURE FLUX QUANTUM AND CHIRAL ANOMALY FOR NEGATIVE CHEMICAL POTENTIAL

In this Appendix, we calculate the Berry curvature flux quantum for each Fermi surface and discuss the chiral anomaly for Fermi energies below the Kramers-Weyl node, i.e.,  $\mu < 0$ . We start by calculating the Berry curvature flux quantum for the FSs. The Berry curvature flux through any FS is defined as  $\mathcal{C}_\lambda = \frac{1}{2\pi} \int_{\text{FS}} d\mathbf{S} \cdot \boldsymbol{\Omega}_\lambda$ , where  $d\mathbf{S}$  is the elemental surface area of the FS. Using the divergence theorem, and capturing the Fermi surface via the Heaviside step function  $[\Theta(\mu - \epsilon_\lambda)]$ , we have

$$\begin{aligned} \mathcal{C}_\lambda &= \frac{1}{2\pi} \int d\mathbf{k} \nabla_{\mathbf{k}} \cdot \boldsymbol{\Omega}_\lambda \Theta(\mu - \epsilon_\lambda) \\ &= -\frac{1}{2\pi} \int d\mathbf{k} \boldsymbol{\Omega}_\lambda \cdot \nabla_{\mathbf{k}} \Theta(\mu - \epsilon_\lambda) \\ &= \frac{\hbar}{2\pi} \int d\mathbf{k} \boldsymbol{\Omega}_\lambda \cdot \mathbf{v}_\lambda \delta(\mu - \epsilon_\lambda). \end{aligned} \quad (\text{B1})$$

TABLE I. The space groups and the point groups for topologically nontrivial chiral crystals hosting Kramers-Weyl fermions with chiral charge  $\pm 1$ . Some material examples, along with the form of the symmetry-allowed SOC terms in the vicinity of the Kramers-Weyl points for each space group, are also presented.

Space group	Point group (Laue class)	Material	SOC term
1	$C_1(1)$	$\text{Li}_6\text{CuB}_4\text{O}_{10}$	$(\alpha_1 k_x + \alpha_2 k_y + \alpha_3 k_z)\sigma_x + (\alpha_4 k_x + \alpha_5 k_y + \alpha_6 k_z)\sigma_y + (\alpha_7 k_x + \alpha_8 k_y + \alpha_9 k_z)\sigma_z$
3–5	$C_2(2)$	$\text{Pb}_3\text{GeO}_5$	$(\alpha_1 k_x + \alpha_2 k_y)\sigma_x + (\alpha_3 k_x + \alpha_4 k_y)\sigma_y + \alpha_5 k_z \sigma_z$
16–24	$D_2(222)$	$\text{AIPS}_4$	$\alpha_1 k_x \sigma_x + \alpha_2 k_y \sigma_y + \alpha_3 k_z \sigma_z$
143–146	$C_3(3)$	$\beta\text{-Ag}_3\text{IS}$	
75–80	$C_4(4)$	$\text{BaCu}_2\text{Te}_2\text{O}_6\text{Cl}_2$	$(\alpha_1 k_x + \alpha_2 k_y)\sigma_x + (\alpha_1 k_y - \alpha_2 k_x)\sigma_y + \alpha_3 k_z \sigma_z$
168–173	$C_6(6)$	$\alpha\text{-In}_2\text{Se}_3$	
149–155	$D_3(32)$	$\text{Ag}_3\text{BO}_3$	
89–98	$D_4(422)$	$\text{CdAs}_2$	$\alpha_1(k_x \sigma_x + k_y \sigma_y) + \alpha_2 k_z \sigma_z$
177–182	$D_6(622)$	$\text{NbGe}_2$	
195–199	$T(23)$	$\text{K}_2\text{Sn}_2\text{O}_3, \beta\text{-RhSi}$	$\alpha_1(k_x \sigma_x + k_y \sigma_y + k_z \sigma_z)$
207–214	$O(432)$	$\text{BaSi}_2, \text{SrSi}_2$	

Note that in the zero-temperature limit, the above expression reduces to the electrical chiral anomaly coefficient defined in Eq. (10). Below, we explicitly calculate the  $C_\lambda$ .

*Case I* ( $\mu > 0$ ). For  $\mu > 0$ , there are two Fermi wave vectors  $k_\lambda^F = -\lambda k_\alpha + \sqrt{k_\alpha^2 + 2m\mu/\hbar^2}$  with  $\lambda = \pm$ , corresponding to two FSs of the two bands. The  $k_+^F$  ( $k_-^F$ ) corresponds to the inner (outer) FS. Now, using the expressions of  $v_\lambda$ ,  $\Omega_\lambda$ , and the  $\delta$ -function property,  $C_\lambda$  for each band  $\lambda$  becomes

$$\begin{aligned} C_\lambda &= \frac{\hbar}{2\pi} \int dk \frac{-\lambda}{2k^2} \left( \frac{\hbar k}{m} + \lambda \frac{\alpha}{\hbar} \right) \delta(\mu - \epsilon_\lambda), \\ &= -\lambda \int dk \left( \frac{\hbar^2 k}{m} + \lambda \alpha \right) \frac{\delta(k_\lambda^F - k)}{|\epsilon'_\lambda|}. \end{aligned} \quad (\text{B2})$$

Here,  $\epsilon'_\lambda$  is the first derivative of  $\epsilon_\lambda$  with respect to  $k$ . Evaluating this integral yields  $C_\lambda = -\lambda$ .

*Case II* ( $\mu < 0$ ). For  $\mu < 0$ , there is only one Fermi surface corresponding to the  $\lambda = -1$  band. However, due to the nonmonotonic band dispersion (see Fig. 4), the Fermi surface contains both holelike carriers, as well as electronlike

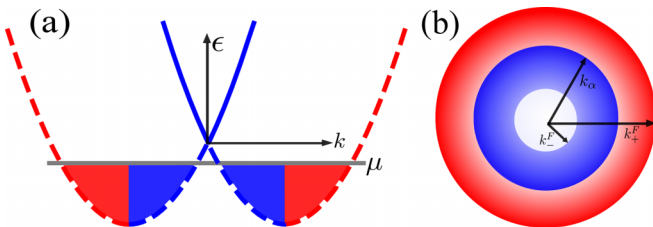


FIG. 4. (a) The band dispersion and the Brillouin zone partitioning for the  $\lambda = -1$  band of a 3D SOC system. For the blue-shaded region with negative-band velocity, the Berry curvature flux is  $-1$ , while the Berry curvature flux is  $+1$  for the red-shaded region with positive-band velocity. (b) The corresponding cross section of the Fermi surface for  $\mu < 0$  for the  $\lambda = -1$  band, highlighting the two partitions Fermi pockets.

carriers. In the region near the nodal point, the band velocity is negative, while in other regions, the band velocity is positive. As a result, we have regions within the same Fermi surface that have opposite signs of the chiral magnetic velocity ( $\propto v_\lambda \cdot \Omega_\lambda$ ). This ensures that the Berry curvature flux through the entire FS calculated using Eq. (B1) is zero. This is consistent with the  $\mu > 0$  case, in which the sum of the Berry curvature flux through the Fermi surfaces of two distinct bands is zero.

We show the partitioning of the FS in Fig 4, with the blue and red regions capturing the holelike and electronlike quasiparticles. Here, the  $\chi$  is used as the index for denoting the inner (outer) region of the FS, with  $\chi = -1$  for the blue region ( $\chi = +1$  for the red region). To calculate the Berry curvature flux using Eq. (B1), we first compute the Fermi wave vectors corresponding to the two different regions of the Fermi pocket of the  $\lambda = -1$  band. The Fermi wave vectors corresponding to the inner ( $\chi = -1$ ) and outer ( $\chi = +1$ ) boundaries of the Fermi pocket are given by  $k_\chi^F = k_\alpha + \chi \sqrt{k_\alpha^2 + 2m\mu/\hbar^2}$ . Recall that  $k_\alpha = m\alpha/\hbar^2$  corresponds to the minima in the energy of the  $\lambda = -1$  band. The  $\chi = -$  ( $+$ ) region of the Fermi pocket corresponds the  $k_-^F < k < k_\alpha$  ( $k_\alpha < k < k_+^F$ ). These regions are represented by blue and red colors, respectively, in Fig. 4. For  $\lambda = -1$  band, the  $C_\lambda$  is given by

$$C_\lambda = \frac{\hbar}{2\pi} \int dk \frac{1}{2k^2} \left( \frac{\hbar k}{m} - \frac{\alpha}{\hbar} \right) \delta(\mu - \epsilon_-). \quad (\text{B3})$$

Now, for either of the two regions, the above equation reduces to

$$C_\lambda^\chi = \int dk \left( \frac{\hbar^2 k}{m} - \alpha \right) \frac{\delta(k_\chi^F - k)}{|\epsilon'_-|}. \quad (\text{B4})$$

As the band velocity  $\epsilon'_- = \hbar^2 k/m - \alpha$  is negative (positive) for the region with  $k_-^F < k < k_\alpha$  ( $k_\alpha < k < k_+^F$ ), Eq. (B4) yields  $C_\lambda^\chi = \chi$ . We note again that the sign of  $C_\lambda^\chi$  is essentially tied to the sign of the chiral magnetic velocity proportional to the  $(v_\lambda \cdot \Omega_\lambda)$  term. The partitioning of the Brillouin zone,

as per the sign of the chiral magnetic velocity, allows one to define two regions of FS with opposite Berry curvature flux quantum. This had been used in Ref. [64] to discuss the continuity equation and the associated electrical chiral anomaly for  $\mu < 0$ , on the same footing as we have discussed for  $\mu > 0$  [64] in the main text. However, the case of  $\mu < 0$  is even more interesting compared to the  $\mu > 0$  case, as the carriers with opposite Berry curvature flux or opposite chirality reside on the same Fermi pocket. This is an example of the chiral anomaly arising from the chiral carriers, both of which reside on the same Fermi surface.

Having discussed the chiral anomaly for  $\mu < 0$ , we conclude this Appendix with a small discussion on the chirality of Weyl-type nodes and the Berry curvature flux quantum. For the WSM, the Berry curvature flux through the FS of a node represents the ‘‘chirality’’ of that node, irrespective of the conduction or the valence band. This is easily seen because, in the  $m \rightarrow \infty$  limit, the Hamiltonian in Eq. (1) reduces to the Hamiltonian for a single Weyl node  $\mathcal{H}_{\text{WSM}}$ . In contrast to the bands of Hamiltonian in Eq. (1), both bands of  $\mathcal{H}_{\text{WSM}}$  are monotonous, and only one FS exists at any particular energy in the vicinity of a nodal point. Then a straightforward calculation following Eq. (B2) yields  $C_\lambda = -\text{sign}(\alpha)$  for both the conduction and valence bands of  $\mathcal{H}_{\text{WSM}}$ . Because the  $C_\lambda$  depends on the sign of  $\alpha$ , the Berry curvature flux quantum becomes opposite for opposite chirality nodes where  $\alpha$  has the opposite sign. This establishes that for WSM, the chirality of each Weyl node can be represented as the Berry curvature flux quantum through the node [5,24,78,98]. However, for the Kramers-Weyl nodes, the Berry curvature flux quantum and the chirality of the node are not identical. The chirality of the Kramers-Weyl nodes depends on the sign of  $\alpha$  for Hamiltonian (1), which is specific to a given TRIM point of the material [67].

### APPENDIX C: CALCULATION OF EQUILIBRIUM CURRENTS

In this Appendix, we derive the expressions of the equilibrium currents obtained in Eqs. (8a) and (8b). In the presence of only a magnetic field, the velocity of the center of mass of the wave packets for the carriers in each band is given by  $\dot{\mathbf{r}}_\lambda = D_\lambda[\mathbf{v}_\lambda + \frac{e}{\hbar}(\mathbf{v}_\lambda \cdot \boldsymbol{\Omega}_\lambda)\mathbf{B}]$ . The equilibrium charge current for the FS  $\lambda$  (corresponding to each band) is given by

$$\mathbf{j}_{e,\text{eq}}^\lambda = -e \int [d\mathbf{k}] D_\lambda^{-1} \dot{\mathbf{r}} f_\lambda = -e \mathbf{B} \int [d\mathbf{k}] \frac{e}{\hbar} (\mathbf{v}_\lambda \cdot \boldsymbol{\Omega}_\lambda) f_\lambda. \quad (\text{C1})$$

Here, we have used the fact that the band velocity  $\mathbf{v}_\lambda$  does not contribute to the equilibrium current (due to angular integration being zero). Now, we use the identity  $\nabla_{\mathbf{k}} \cdot (\epsilon_\lambda \boldsymbol{\Omega}_\lambda) = \nabla_{\mathbf{k}} \epsilon_\lambda \cdot \boldsymbol{\Omega}_\lambda + \epsilon_\lambda \nabla_{\mathbf{k}} \cdot \boldsymbol{\Omega}_\lambda$  to express the above equation as

$$\mathbf{j}_{e,\text{eq}}^\lambda = -\frac{e^2 \mathbf{B}}{\hbar^2} \int [d\mathbf{k}] [\nabla_{\mathbf{k}} \cdot (\epsilon_\lambda \boldsymbol{\Omega}_\lambda) - \epsilon_\lambda \nabla_{\mathbf{k}} \cdot \boldsymbol{\Omega}_\lambda] f_\lambda \quad (\text{C2})$$

$$= -\frac{e^2 \mathbf{B}}{\hbar^2} \int [d\mathbf{k}] \nabla_{\mathbf{k}} \cdot (\epsilon_\lambda \boldsymbol{\Omega}_\lambda) f_\lambda \quad (\text{C3})$$

$$= \frac{e^2}{\hbar^2} \mathbf{B} \int [d\mathbf{k}] \epsilon_\lambda \boldsymbol{\Omega}_\lambda \cdot \hat{\mathbf{k}} \frac{\partial f_\lambda}{\partial \mathbf{k}} \quad (\text{C4})$$

$$\begin{aligned} &= -e \mathbf{B} \int [d\mathbf{k}] (\mu + \epsilon_\lambda - \mu) \frac{e}{\hbar} (\mathbf{v}_\lambda \cdot \boldsymbol{\Omega}_\lambda) \left( -\frac{\partial f_\lambda}{\partial \epsilon_\lambda} \right) \\ &= -e (\mu C_0^\lambda + k_B T C_1^\lambda) \mathbf{B}. \end{aligned} \quad (\text{C5})$$

To evaluate Eq. (C3), we have used the fact that  $\nabla_{\mathbf{k}} \cdot \boldsymbol{\Omega}_\lambda = \pm 2\pi \delta^3(\mathbf{k})$  for a system with doubly degenerate band-touching point with linear dispersion. This makes the last integral of Eq. (C2) to be zero. To obtain Eq. (C4) from (C3), we have used integration by parts. Here, we have defined  $C_\nu^\lambda$  as

$$C_\nu^\lambda = \int [d\mathbf{k}] \frac{e}{\hbar} \mathbf{v}_\lambda \cdot \boldsymbol{\Omega}_\lambda \left( \frac{\epsilon - \mu}{k_B T} \right)^\nu \left( -\frac{\partial f_\lambda}{\partial \epsilon_\lambda} \right). \quad (\text{C6})$$

These can also be rewritten in terms of  $C_\lambda$  given in Eq. (10). The energy current  $\mathbf{j}_{\epsilon,\text{eq}}^\lambda$  can be evaluated in a similar manner.

Finally, we derive the spatial divergence of the equilibrium particle and energy currents, which will be used in the following Appendix. Following Eq. (C1), the equilibrium particle current is given by  $\mathbf{J}_e^\lambda = \int [d\mathbf{k}] \frac{e}{\hbar} (\mathbf{v}_\lambda \cdot \boldsymbol{\Omega}_\lambda) \mathbf{B} f_\lambda$ . The divergence of the equilibrium particle current becomes

$$\begin{aligned} \nabla_r \cdot \mathbf{J}_e^\lambda &= \nabla_r \cdot \left[ \mathbf{B} \int [d\mathbf{k}] \frac{e}{\hbar} (\mathbf{v}_\lambda \cdot \boldsymbol{\Omega}_\lambda) f_\lambda \right] \\ &= \mathbf{B} \cdot \int [d\mathbf{k}] \frac{e}{\hbar} (\mathbf{v}_\lambda \cdot \boldsymbol{\Omega}_\lambda) \nabla_r T \frac{\epsilon_\lambda - \mu}{T} (-\partial_\epsilon f_\lambda) \\ &= k_B C_1^\lambda \nabla T \cdot \mathbf{B}. \end{aligned} \quad (\text{C7})$$

Here, we have the relation  $\nabla_r f_\lambda = \nabla T \frac{\epsilon_\lambda - \mu}{T} (-\partial_\epsilon f_\lambda)$ , and the definition of  $C_1^\lambda$ .

Similarly, for the divergence of the equilibrium energy current, we start with

$$\begin{aligned} \nabla_r \cdot \mathbf{J}_\epsilon^\lambda &= \nabla_r \cdot \left[ \mathbf{B} \int [d\mathbf{k}] \frac{e}{\hbar} (\mathbf{v}_\lambda \cdot \boldsymbol{\Omega}_\lambda) \epsilon_\lambda f_\lambda \right] \\ &= \mathbf{B} \cdot \int [d\mathbf{k}] \frac{e}{\hbar} (\mathbf{v}_\lambda \cdot \boldsymbol{\Omega}_\lambda) (\mu + \epsilon_\lambda - \mu) \\ &\quad \times \nabla_r T \frac{\epsilon_\lambda - \mu}{T} (-\partial_\epsilon f_\lambda) \\ &= \mu k_B \mathbf{B} \cdot \nabla_r T \int [d\mathbf{k}] \frac{e}{\hbar} (\mathbf{v}_\lambda \cdot \boldsymbol{\Omega}_\lambda) \frac{\epsilon_\lambda - \mu}{k_B T} (-\partial_\epsilon f_\lambda) \\ &\quad + k_B^2 T \mathbf{B} \cdot \nabla_r T \int [d\mathbf{k}] \frac{e}{\hbar} (\mathbf{v}_\lambda \cdot \boldsymbol{\Omega}_\lambda) \\ &\quad \times \left( \frac{\epsilon_\lambda - \mu}{k_B T} \right)^2 (-\partial_\epsilon f_\lambda) \\ &= (\mu k_B C_1^\lambda + k_B^2 T C_2^\lambda) \nabla T \cdot \mathbf{B}. \end{aligned} \quad (\text{C8})$$

We will use these expressions in the next Appendix for deriving the particle and energy continuity equations.

### APPENDIX D: DERIVATION OF PARTICLE AND ENERGY CONTINUITY EQUATIONS

Within the relaxation time approximation, the Boltzmann transport equation, including the inter-Fermi-surface scattering term, is given by

$$\frac{\partial g_\lambda}{\partial t} + \dot{\mathbf{r}}_\lambda \cdot \nabla_r g_\lambda + \dot{\mathbf{k}}_\lambda \cdot \nabla_k g_\lambda = -\frac{g_\lambda - \bar{g}_\lambda}{\tau} - \frac{\bar{g}_\lambda - f_\lambda}{\tau_\nu}. \quad (\text{D1})$$

Using the equation of motion of Eqs. (6a) and (6b) in the above equation, we obtain

$$\frac{\partial g_\lambda}{\partial t} + D_\lambda \left[ \mathbf{v}_\lambda + \frac{e}{\hbar} \mathbf{E} \times \boldsymbol{\Omega}_\lambda + \frac{e}{\hbar} (\mathbf{v}_\lambda \cdot \boldsymbol{\Omega}_\lambda) \mathbf{B} \right] \cdot \nabla_r g_\lambda - D_\lambda \left[ e\mathbf{E} + e\mathbf{v}_\lambda \times \mathbf{B} + \frac{e^2}{\hbar} (\mathbf{E} \cdot \mathbf{B}) \boldsymbol{\Omega}_\lambda \right] \cdot \nabla_k g_\lambda = -\frac{g_\lambda - \bar{g}_\lambda}{\tau} - \frac{\bar{g}_\lambda - f_\lambda}{\tau_v}. \quad (\text{D2})$$

Integrating the above equation over all the momentum states with  $\int [d\mathbf{k}] D_\lambda^{-1}$ , for linear order response, we obtain

$$\begin{aligned} \frac{\partial \mathcal{N}^\lambda}{\partial t} + \int [d\mathbf{k}] \mathbf{v}_\lambda \cdot \nabla T \left( \frac{\epsilon_\lambda - \mu}{T} \right) (-\partial_\epsilon f_\lambda) + \int [d\mathbf{k}] \frac{e}{\hbar} (\mathbf{E} \times \boldsymbol{\Omega}_\lambda) \cdot \nabla T \left( \frac{\epsilon_\lambda - \mu}{T} \right) (-\partial_\epsilon f_\lambda) \\ + \int [d\mathbf{k}] \frac{e}{\hbar} (\mathbf{v}_\lambda \cdot \boldsymbol{\Omega}_\lambda) \mathbf{B} \cdot \nabla T \left( \frac{\epsilon_\lambda - \mu}{T} \right) (-\partial_\epsilon f_\lambda) + \int [d\mathbf{k}] e\mathbf{E} \cdot \mathbf{v}_\lambda (-\partial_\epsilon f_\lambda) + \int [d\mathbf{k}] e(\mathbf{v}_\lambda \times \mathbf{B}) \cdot \mathbf{v}_\lambda (-\partial_\epsilon f_\lambda) \\ + \int [d\mathbf{k}] \frac{e^2}{\hbar} (\mathbf{E} \cdot \mathbf{B}) \boldsymbol{\Omega}_\lambda \cdot \mathbf{v}_\lambda (-\partial_\epsilon f_\lambda) = -\frac{\mathcal{N}^\lambda - \mathcal{N}_0^\lambda}{\tau_v}. \end{aligned} \quad (\text{D3})$$

Here, we have used the relation  $\nabla_r f_\lambda = \nabla T \frac{\epsilon_\lambda - \mu}{T} (-\partial_\epsilon f_\lambda)$ , and  $\nabla_k f_\lambda = \hbar \mathbf{v}_\lambda (\partial_\epsilon f_\lambda)$ . In Eq. (D3), we have defined  $\{\mathcal{N}_0^\lambda, \mathcal{N}^\lambda\} = \int [d\mathbf{k}] D_\lambda^{-1} \{f_\lambda, g_\lambda\}$ , which represents the total particle number density in each FS before and after applying the perturbing fields. Since the intra-Fermi-surface scattering does not change the number of particles, the  $\tau$ -dependent intra-Fermi-surface term in the right-hand side of Eq. (D3) vanishes. The second term in both the first and second lines of Eq. (D3) vanishes owing to the angular integration over the polar angle  $\theta$ , and the isotropic energy dispersion of Hamiltonian (1). The third term in the first line represents the mixed nonlinear response as it contains both the perturbing field  $\mathbf{E}$  and  $\nabla T$ . We ignore this term as we focus on the linear response regime. The third term in the second line is identically zero as it involves the vector triple product, with two of them being identical. Accounting for these, we are left with the equation

$$\frac{\partial \mathcal{N}^\lambda}{\partial t} + k_B \nabla T \cdot \mathbf{B} \int [d\mathbf{k}] \frac{e}{\hbar} (\mathbf{v}_\lambda \cdot \boldsymbol{\Omega}_\lambda) \left( \frac{\epsilon_\lambda - \mu}{k_B T} \right) (-\partial_\epsilon f_\lambda) + e\mathbf{E} \cdot \mathbf{B} \int [d\mathbf{k}] \frac{e}{\hbar} (\mathbf{v}_\lambda \cdot \boldsymbol{\Omega}_\lambda) (-\partial_\epsilon f_\lambda) = -\frac{\mathcal{N}^\lambda - \mathcal{N}_0^\lambda}{\tau_v}. \quad (\text{D4})$$

Using the definition of  $C_1^\lambda$  of Eq. (10), the second term becomes  $k_B C_1^\lambda \nabla T \cdot \mathbf{B}$ . Using Eq. (C7) we write this term as  $\nabla_r \cdot \mathbf{J}_e^\lambda$ . The first term in Eq. (D4) can be rewritten as  $e\mathbf{E} \cdot \mathbf{B} C_0^\lambda$  using Eq. (10). Combining these, we arrive at Eq. (16). The derivation of the energy continuity equation (17) is very similar to that of particle continuity equation (16). To evaluate the energy continuity equation, we integrate Eq. (D2) over all the momentum states weighted by energy expression  $\epsilon_\lambda$  (i.e.,  $\int [d\mathbf{k}] D_\lambda^{-1} \epsilon_\lambda$ ):

$$\begin{aligned} \frac{\partial \mathcal{E}^\lambda}{\partial t} + \int [d\mathbf{k}] \epsilon_\lambda \mathbf{v}_\lambda \cdot \nabla T \left( \frac{\epsilon_\lambda - \mu}{T} \right) (-\partial_\epsilon f_\lambda) + \int [d\mathbf{k}] \epsilon_\lambda \frac{e}{\hbar} (\mathbf{E} \times \boldsymbol{\Omega}_\lambda) \cdot \nabla T \left( \frac{\epsilon_\lambda - \mu}{T} \right) (-\partial_\epsilon f_\lambda) \\ + \int [d\mathbf{k}] \epsilon_\lambda \frac{e}{\hbar} (\mathbf{v}_\lambda \cdot \boldsymbol{\Omega}_\lambda) \mathbf{B} \cdot \nabla T \left( \frac{\epsilon_\lambda - \mu}{T} \right) (-\partial_\epsilon f_\lambda) + \int [d\mathbf{k}] \epsilon_\lambda e\mathbf{E} \cdot \mathbf{v}_\lambda (-\partial_\epsilon f_\lambda) + \int [d\mathbf{k}] \epsilon_\lambda e(\mathbf{v}_\lambda \times \mathbf{B}) \cdot \mathbf{v}_\lambda (-\partial_\epsilon f_\lambda) \\ + \int [d\mathbf{k}] \epsilon_\lambda \frac{e^2}{\hbar} (\mathbf{E} \cdot \mathbf{B}) \boldsymbol{\Omega}_\lambda \cdot \mathbf{v}_\lambda (-\partial_\epsilon f_\lambda) = -\frac{\mathcal{E}^\lambda - \mathcal{E}_0^\lambda}{\tau_v}. \end{aligned} \quad (\text{D5})$$

Using arguments similar to those used for Eq. (D3), the corresponding terms also vanish here. This yields the equation

$$\frac{\partial \mathcal{E}^\lambda}{\partial t} + k_B \nabla T \cdot \mathbf{B} \int [d\mathbf{k}] \frac{e}{\hbar} (\mathbf{v}_\lambda \cdot \boldsymbol{\Omega}_\lambda) \epsilon_\lambda \left( \frac{\epsilon_\lambda - \mu}{k_B T} \right) (-\partial_\epsilon f_\lambda) + e\mathbf{E} \cdot \mathbf{B} \int [d\mathbf{k}] \frac{e}{\hbar} (\mathbf{v}_\lambda \cdot \boldsymbol{\Omega}_\lambda) \epsilon_\lambda (-\partial_\epsilon f_\lambda) = -\frac{\mathcal{E}^\lambda - \mathcal{E}_0^\lambda}{\tau_v}. \quad (\text{D6})$$

The above equation can be rewritten as

$$\begin{aligned} \frac{\partial \mathcal{E}^\lambda}{\partial t} + k_B \nabla T \cdot \mathbf{B} \int [d\mathbf{k}] \frac{e}{\hbar} (\mathbf{v}_\lambda \cdot \boldsymbol{\Omega}_\lambda) (\epsilon_\lambda - \mu + \mu) \left( \frac{\epsilon_\lambda - \mu}{k_B T} \right) (-\partial_\epsilon f_\lambda) + e\mathbf{E} \cdot \mathbf{B} \int [d\mathbf{k}] \frac{e}{\hbar} (\mathbf{v}_\lambda \cdot \boldsymbol{\Omega}_\lambda) (\epsilon_\lambda - \mu + \mu) (-\partial_\epsilon f_\lambda) \\ = -\frac{\mathcal{E}^\lambda - \mathcal{E}_0^\lambda}{\tau_v} \end{aligned} \quad (\text{D7})$$

$$\begin{aligned} \Rightarrow \frac{\partial \mathcal{E}^\lambda}{\partial t} + k_B^2 T \nabla T \cdot \mathbf{B} \int [d\mathbf{k}] \frac{e}{\hbar} (\mathbf{v}_\lambda \cdot \boldsymbol{\Omega}_\lambda) \left( \frac{\epsilon_\lambda - \mu}{k_B T} \right)^2 (-\partial_\epsilon f_\lambda) + \mu k_B \nabla T \cdot \mathbf{B} \int [d\mathbf{k}] \frac{e}{\hbar} (\mathbf{v}_\lambda \cdot \boldsymbol{\Omega}_\lambda) \left( \frac{\epsilon_\lambda - \mu}{k_B T} \right) (-\partial_\epsilon f_\lambda) \\ + e\mathbf{E} \cdot \mathbf{B} k_B T \int [d\mathbf{k}] \frac{e}{\hbar} (\mathbf{v}_\lambda \cdot \boldsymbol{\Omega}_\lambda) \left( \frac{\epsilon_\lambda - \mu}{k_B T} \right) (-\partial_\epsilon f_\lambda) + \mu e\mathbf{E} \cdot \mathbf{B} \int [d\mathbf{k}] \frac{e}{\hbar} (\mathbf{v}_\lambda \cdot \boldsymbol{\Omega}_\lambda) (-\partial_\epsilon f_\lambda) = -\frac{\mathcal{E}^\lambda - \mathcal{E}_0^\lambda}{\tau_v}. \end{aligned} \quad (\text{D8})$$

Using the definitions of  $C_\nu^\lambda$ , the above equation reduces to

$$\frac{\partial \mathcal{E}^\lambda}{\partial t} + (\mu C_0^\lambda + k_B T C_1^\lambda) e\mathbf{E} \cdot \mathbf{B} + \nabla_r \cdot \mathbf{J}_\mathcal{E}^\lambda = -\frac{\mathcal{E}^\lambda - \mathcal{E}_0^\lambda}{\tau_v}. \quad (\text{D9})$$

Here, we have used Eq. (C8) to write  $\nabla_r \cdot \mathbf{J}_\mathcal{E}^\lambda = (\mu k_B C_1^\lambda + k_B^2 T C_2^\lambda) \nabla T \cdot \mathbf{B}$ .

### APPENDIX E: DETAILS OF SPIN CURRENT CALCULATIONS

To calculate the spin current proportional to the  $\mathbf{E} \cdot \mathbf{B}$  (or  $\nabla T \cdot \mathbf{B}$ ), we consider the band velocity term of Eq. (6a) and calculate the spin current operator. The band velocity operator along the  $i$  direction is given by  $\hat{v}_i = \frac{\hbar k_i}{m} \sigma_0 + \frac{\alpha}{\hbar} \sigma_i$ . Without loss of generality, here we show the calculation of spin current in the  $x$  direction. Using the expressions of the eigenstates and the spin current operator given in the main text, we obtain  $\langle u_\lambda | \hat{J}_x^{s_x} | u_\lambda \rangle = (\alpha/\hbar + \lambda \hbar k_x \sin \theta_k \cos \phi_k/m)$ . Now, the chiral-anomaly-induced spin current is given by

$$j_x^{s_x} = \tau_v \sum_\lambda \int [dk] \left( \frac{\alpha}{\hbar} + \lambda \frac{\hbar k_x}{m} \sin \theta_k \cos \phi_k \right) \times \left( \delta\mu_\lambda + \frac{\epsilon_\lambda - \mu}{T} \delta T_\lambda \right) \left( -\frac{\partial f_\lambda}{\partial \epsilon_\lambda} \right). \quad (\text{E1})$$

In the  $\beta\mu \rightarrow \infty$  limit, writing the expressions of  $\delta\mu_\lambda$  and  $\delta T_\lambda$  explicitly, we have

$$j_x^{s_x} = \tau_v \sum_\lambda \left[ \frac{\mathcal{D}_1^\lambda C_0^\lambda}{\mathcal{D}_2^\lambda \mathcal{D}_0^\lambda} \mathcal{L}_1 - \frac{C_0^\lambda}{\mathcal{D}_0^\lambda} \mathcal{L}_0 \right] e\mathbf{E} \cdot \mathbf{B} - \left[ \frac{\mathcal{D}_1^\lambda C_2^\lambda}{\mathcal{D}_2^\lambda \mathcal{D}_0^\lambda} \mathcal{L}_0 - \frac{C_2^\lambda}{\mathcal{D}_2^\lambda} \mathcal{L}_1 \right] k_B \nabla T \cdot \mathbf{B}. \quad (\text{E2})$$

The definition of  $\mathcal{L}_\nu$  is given in the main text. We evaluate the  $\mathcal{L}_\nu$  using the Sommerfeld approximation in the  $\mu \gg k_B T$  limit. We obtain the expressions

$$\mathcal{L}_0 = -\lambda \frac{m^2 \alpha^2}{6\pi^2 \hbar^5} \frac{[\tilde{\mu} - \tilde{\mu}^2 + 2(1 + \tilde{\mu})]}{1 + \tilde{\mu}}, \quad (\text{E3})$$

$$\mathcal{L}_1 = \frac{k_B T}{9\hbar^3} \frac{(-\lambda + \sqrt{1 + \tilde{\mu}})[\lambda(2 + \tilde{\mu}) + \sqrt{1 + \tilde{\mu}}]}{(1 + \tilde{\mu})^{3/2}}. \quad (\text{E4})$$

Using these expressions along with  $C_\nu^\lambda$  and  $\mathcal{D}_\nu^\lambda$  in Eq. (E2), we obtain the spin conductivities of Eqs. (38) and (39). Following a similar procedure, we can calculate other spin currents.

We show that due to rotational symmetry  $j_i^{s_j} = 0$  for  $i \neq j$ . Without loss of generality, we will explicitly show the calculation for  $j_x^{s_z}$ . The expectation value of the spin current operator  $\hat{J}_x^{s_z}$  is given by  $\langle u_\lambda | \hat{J}_x^{s_z} | u_\lambda \rangle = \lambda \frac{p}{2m} \sin 2\theta_k \cos \phi_k$ . Now, as the distribution function is independent of  $\theta_k$  and  $\phi_k$ , so the angular integration over  $\phi_k$  of the  $\langle u_\lambda | \hat{J}_x^{s_z} | u_\lambda \rangle$  yields  $j_x^{s_z} = 0$ . Similarly, all the spin currents with spin polarization perpendicular to the propagation velocity can be easily shown to be zero due to the vanishing angular integration over  $\phi_k$ .

- 
- [1] S. L. Adler, *Phys. Rev.* **177**, 2426 (1969).  
[2] H. Nielsen and M. Ninomiya, *Nucl. Phys. B* **185**, 20 (1981).  
[3] H. Nielsen and M. Ninomiya, *Nucl. Phys. B* **193**, 173 (1981).  
[4] H. Nielsen and M. Ninomiya, *Phys. Lett. B* **130**, 389 (1983).  
[5] D. T. Son and B. Z. Spivak, *Phys. Rev. B* **88**, 104412 (2013).  
[6] S. A. Parameswaran, T. Grover, D. A. Abanin, D. A. Pesin, and A. Vishwanath, *Phys. Rev. X* **4**, 031035 (2014).  
[7] J. Xiong, S. K. Kushwaha, T. Liang, J. W. Krizan, M. Hirschberger, W. Wang, R. J. Cava, and N. P. Ong, *Science* **350**, 413 (2015).  
[8] A. A. Burkov, *Phys. Rev. B* **96**, 041110(R) (2017).  
[9] C.-L. Zhang, S.-Y. Xu, I. Belopolski, Z. Yuan, Z. Lin, B. Tong, G. Bian, N. Alidoust, C.-C. Lee, S.-M. Huang, T.-R. Chang, G. Chang, C.-H. Hsu, H.-T. Jeng, M. Neupane, D. S. Sanchez, H. Zheng, J. Wang, H. Lin, C. Zhang *et al.*, *Nat. Commun.* **7**, 10735 (2016).  
[10] Q. Li, D. E. Kharzeev, C. Zhang, Y. Huang, I. Pletikosić, A. V. Fedorov, R. D. Zhong, J. A. Schneeloch, G. D. Gu, and T. Valla, *Nat. Phys.* **12**, 550 (2016).  
[11] R. D. dos Reis, M. O. Ajeesh, N. Kumar, F. Arnold, C. Shekhar, M. Naumann, M. Schmidt, M. Nicklas, and E. Hassinger, *New J. Phys.* **18**, 085006 (2016).  
[12] S. Nandy, G. Sharma, A. Taraphder, and S. Tewari, *Phys. Rev. Lett.* **119**, 176804 (2017).  
[13] Y. Li, Z. Wang, P. Li, X. Yang, Z. Shen, F. Sheng, X. Li, Y. Lu, Y. Zheng, and Z.-A. Xu, *Front. Phys.* **12**, 127205 (2017).  
[14] N. Kumar, S. N. Guin, C. Felser, and C. Shekhar, *Phys. Rev. B* **98**, 041103(R) (2018).  
[15] K.-S. Kim, H.-J. Kim, and M. Sasaki, *Phys. Rev. B* **89**, 195137 (2014).  
[16] M.-X. Deng, G. Y. Qi, R. Ma, R. Shen, R.-Q. Wang, L. Sheng, and D. Y. Xing, *Phys. Rev. Lett.* **122**, 036601 (2019).  
[17] K. Das and A. Agarwal, *Phys. Rev. B* **99**, 085405 (2019).  
[18] K. Das, S. K. Singh, and A. Agarwal, *Phys. Rev. Res.* **2**, 033511 (2020).  
[19] K. Das and A. Agarwal, *Phys. Rev. B* **100**, 085406 (2019).  
[20] S. Nandy, A. Taraphder, and S. Tewari, *Phys. Rev. B* **100**, 115139 (2019).  
[21] G. Sharma, S. Nandy, and S. Tewari, *Phys. Rev. B* **102**, 205107 (2020).  
[22] C. Xiao, H. Chen, Y. Gao, D. Xiao, A. H. MacDonald, and Q. Niu, *Phys. Rev. B* **101**, 201410(R) (2020).  
[23] K. Das and A. Agarwal, *Phys. Rev. B* **103**, 125432 (2021).  
[24] K. Das and A. Agarwal, *Phys. Rev. Res.* **2**, 013088 (2020).  
[25] D. Mandal, K. Das, and A. Agarwal, *Phys. Rev. B* **106**, 035423 (2022).  
[26] M.-X. Deng, Y.-C. Hu, W. Luo, H.-J. Duan, and R.-Q. Wang, *Phys. Rev. B* **106**, 075139 (2022).  
[27] R. Sen and S. Kar, *J. Phys.: Condens. Matter* **34**, 465601 (2022).  
[28] M.-X. Deng, J.-Y. Ba, R. Ma, W. Luo, R.-Q. Wang, L. Sheng, and D. Y. Xing, *Phys. Rev. Res.* **2**, 033346 (2020).  
[29] C. Zeng, S. Nandy, P. Liu, S. Tewari, and Y. Yao, *Phys. Rev. B* **107**, L081107 (2023).

- [30] F. Hütt, D. Kamenskyi, D. Neubauer, C. Shekhar, C. Felser, M. Dressel, and A. V. Pronin, *Results Phys.* **15**, 102630 (2019).
- [31] P. Hosur and X.-L. Qi, *Phys. Rev. B* **91**, 081106(R) (2015).
- [32] P. E. C. Ashby and J. P. Carbotte, *Phys. Rev. B* **89**, 245121 (2014).
- [33] J. Ma and D. A. Pesin, *Phys. Rev. B* **92**, 235205 (2015).
- [34] T. Morimoto and N. Nagaosa, *Phys. Rev. Lett.* **117**, 146603 (2016).
- [35] J. Behrends, A. G. Grushin, T. Ojanen, and J. H. Bardarson, *Phys. Rev. B* **93**, 075114 (2016).
- [36] A. A. Zyuzin and A. Y. Zyuzin, *Phys. Rev. B* **95**, 085127 (2017).
- [37] M. M. Jadidi, M. Kargarian, M. Mittendorff, Y. Aytac, B. Shen, J. C. König-Otto, S. Winnerl, N. Ni, A. L. Gaeta, T. E. Murphy, and H. D. Drew, *Phys. Rev. B* **102**, 245123 (2020).
- [38] A. Thakur, K. Sadhukhan, and A. Agarwal, *Phys. Rev. B* **97**, 035403 (2018).
- [39] K. Sonowal, A. Singh, and A. Agarwal, *Phys. Rev. B* **100**, 085436 (2019).
- [40] H.-W. Wang, B. Fu, and S.-Q. Shen, *Phys. Rev. B* **104**, L241111 (2021).
- [41] A. V. Andreev and B. Z. Spivak, *Phys. Rev. Lett.* **120**, 026601 (2018).
- [42] K. Landsteiner, E. Megías, and F. Pena-Benitez, *Phys. Rev. Lett.* **107**, 021601 (2011).
- [43] A. Lucas, R. A. Davison, and S. Sachdev, *Proc. Natl. Acad. Sci. USA* **113**, 9463 (2016).
- [44] J. Gooth, A. C. Niemann, T. Meng, A. G. Grushin, K. Landsteiner, B. Gotsmann, F. Menges, M. Schmidt, C. Shekhar, V. Süß, R. Hühne, B. Rellinghaus, C. Felser, B. Yan, and K. Nielsch, *Nature (London)* **547**, 324 (2017).
- [45] M. Stone and J. Kim, *Phys. Rev. D* **98**, 025012 (2018).
- [46] R. Lundgren, P. Laurell, and G. A. Fiete, *Phys. Rev. B* **90**, 165115 (2014).
- [47] M. Hirschberger, S. Kushwaha, Z. Wang, Q. Gibson, S. Liang, C. Belvin, B. A. Bernevig, R. J. Cava, and N. P. Ong, *Nat. Mater.* **15**, 1161 (2016).
- [48] Z. Jia, C. Li, X. Li, J. Shi, Z. Liao, D. Yu, and X. Wu, *Nat. Commun.* **7**, 13013 (2016).
- [49] B. Z. Spivak and A. V. Andreev, *Phys. Rev. B* **93**, 085107 (2016).
- [50] U. Stockert, R. D. dos Reis, M. O. Ajeesh, S. J. Watzman, M. Schmidt, C. Shekhar, J. P. Heremans, C. Felser, M. Baenitz, and M. Nicklas, *J. Phys.: Condens. Matter* **29**, 325701 (2017).
- [51] V. A. Zyuzin, *Phys. Rev. B* **95**, 245128 (2017).
- [52] C. Zeng, S. Nandy, and S. Tewari, *Phys. Rev. B* **105**, 125131 (2022).
- [53] D. Vu, W. Zhang, C. Sahin, M. E. Flatte, N. Trivedi, and J. P. Heremans, *Nat. Mater.* **20**, 1525 (2021).
- [54] D. T. Son and N. Yamamoto, *Phys. Rev. Lett.* **109**, 181602 (2012).
- [55] D. T. Son and N. Yamamoto, *Phys. Rev. D* **87**, 085016 (2013).
- [56] M. A. Stephanov and Y. Yin, *Phys. Rev. Lett.* **109**, 162001 (2012).
- [57] C. Fang, M. J. Gilbert, X. Dai, and B. A. Bernevig, *Phys. Rev. Lett.* **108**, 266802 (2012).
- [58] X. Li, B. Roy, and S. Das Sarma, *Phys. Rev. B* **94**, 195144 (2016).
- [59] Z.-M. Huang, J. Zhou, and S.-Q. Shen, *Phys. Rev. B* **96**, 085201 (2017).
- [60] S. Nandy, C. Zeng, and S. Tewari, *Phys. Rev. B* **104**, 205124 (2021).
- [61] R. M. A. Dantas, F. Peña-Benitez, B. Roy, and P. Surówka, *J. High Energy Phys.* (2018) 069.
- [62] S. Das, K. Das, and A. Agarwal, *Phys. Rev. B* **105**, 235408 (2022).
- [63] L. Lepori, M. Burrello, and E. Guadagnini, *J. High Energy Phys.* **06** (2018) 110.
- [64] S. Cheon, G. Y. Cho, K.-S. Kim, and H.-W. Lee, *Phys. Rev. B* **105**, L180303 (2022).
- [65] L.-L. Gao and X.-G. Huang, *Chin. Phys. Lett.* **39**, 021101 (2022).
- [66] B. Bradlyn, J. Cano, Z. Wang, M. G. Vergniory, C. Felser, R. J. Cava, and B. A. Bernevig, *Science* **353**, aaf5037 (2016).
- [67] G. Chang, B. J. Wieder, F. Schindler, D. S. Sanchez, I. Belopolski, S.-M. Huang, B. Singh, D. Wu, T.-R. Chang, T. Neupert, S.-Y. Xu, H. Lin, and M. Z. Hasan, *Nat. Mater.* **17**, 978 (2018).
- [68] W.-Y. He, X. Y. Xu, and K. T. Law, *Commun. Phys.* **4**, 66 (2021).
- [69] C.-L. Zhang, F. Schindler, H. Liu, T.-R. Chang, S.-Y. Xu, G. Chang, W. Hua, H. Jiang, Z. Yuan, J. Sun, H.-T. Jeng, H.-Z. Lu, H. Lin, M. Z. Hasan, X. C. Xie, T. Neupert, and S. Jia, *Phys. Rev. B* **96**, 165148 (2017).
- [70] N. B. M. Schröter, D. Pei, M. G. Vergniory, Y. Sun, K. Manna, F. de Juan, J. A. Krieger, V. Süß, M. Schmidt, P. Dudin, B. Bradlyn, T. K. Kim, T. Schmitt, C. Cacho, C. Felser, V. N. Strocov, and Y. Chen, *Nat. Phys.* **15**, 759 (2019).
- [71] W. Tan, X. Jiang, Y. Li, X. Wu, J. Wang, and B. Huang, *Adv. Funct. Mater.* **32**, 2208023 (2022).
- [72] Z. Rao, H. Li, T. Zhang, S. Tian, C. Li, B. Fu, C. Tang, L. Wang, Z. Li, W. Fan, J. Li, Y. Huang, Z. Liu, Y. Long, C. Fang, H. Weng, Y. Shi, H. Lei, Y. Sun, T. Qian *et al.*, *Nature (London)* **567**, 496 (2019).
- [73] D. S. Sanchez, I. Belopolski, T. A. Cochran, X. Xu, J.-X. Yin, G. Chang, W. Xie, K. Manna, V. Süß, C.-Y. Huang, N. Alidoust, D. Multer, S. S. Zhang, N. Shumiya, X. Wang, G.-Q. Wang, T.-R. Chang, C. Felser, S.-Y. Xu, S. Jia *et al.*, *Nature (London)* **567**, 500 (2019).
- [74] D. Dutta, B. Ghosh, B. Singh, H. Lin, A. Politano, A. Bansil, and A. Agarwal, *Phys. Rev. B* **105**, 165104 (2022).
- [75] D. Takane, Z. Wang, S. Souma, K. Nakayama, T. Nakamura, H. Oinuma, Y. Nakata, H. Iwasawa, C. Cacho, T. Kim, K. Horiba, H. Kumigashira, T. Takahashi, Y. Ando, and T. Sato, *Phys. Rev. Lett.* **122**, 076402 (2019).
- [76] S. Verma, T. Biswas, and T. K. Ghosh, *Phys. Rev. B* **100**, 045201 (2019).
- [77] O. Pal, B. Dey, and T. K. Ghosh, *J. Phys.: Condens. Matter* **34**, 025702 (2022).
- [78] N. P. Armitage, E. J. Mele, and A. Vishwanath, *Rev. Mod. Phys.* **90**, 015001 (2018).
- [79] J. Kang and J. Zang, *Phys. Rev. B* **91**, 134401 (2015).
- [80] K. V. Samokhin, *Phys. Rev. B* **78**, 144511 (2008).
- [81] D. Xiao, M.-C. Chang, and Q. Niu, *Rev. Mod. Phys.* **82**, 1959 (2010).
- [82] T. Morimoto, S. Zhong, J. Orenstein, and J. E. Moore, *Phys. Rev. B* **94**, 245121 (2016).
- [83] D. Xiao, J. Shi, and Q. Niu, *Phys. Rev. Lett.* **95**, 137204 (2005).
- [84] K. Fukushima, D. E. Kharzeev, and H. J. Warringa, *Phys. Rev. D* **78**, 074033 (2008).

- [85] Q. Li and D. E. Kharzeev, *Nucl. Phys. A* **956**, 107 (2016).
- [86] D. E. Kharzeev, *Prog. Part. Nucl. Phys.* **75**, 133 (2014).
- [87] D. E. Kharzeev, Y. Kikuchi, and R. Meyer, *Eur. Phys. J. B* **91**, 83 (2018).
- [88] S. K. Yip, [arXiv:1508.01010](https://arxiv.org/abs/1508.01010).
- [89] A. A. Burkov, *Phys. Rev. B* **91**, 245157 (2015).
- [90] N. Ashcroft and N. Mermin, *Solid State Physics*, HRW international editions (Holt, Rinehart and Winston, New York, 1976).
- [91] S. Verma, A. Kundu, and T. K. Ghosh, *Phys. Rev. B* **102**, 195208 (2020).
- [92] C. Schindler, S. Galeski, W. Schnelle, R. Wawrzyńczak, W. Abdel-Haq, S. N. Guin, J. Kroder, N. Kumar, C. Fu, H. Borrmann, C. Shekhar, C. Felser, T. Meng, A. G. Grushin, Y. Zhang, Y. Sun, and J. Gooth, *Phys. Rev. B* **101**, 125119 (2020).
- [93] P. Kapri, B. Dey, and T. K. Ghosh, *Phys. Rev. B* **103**, 165401 (2021).
- [94] Y. Gao, [arXiv:2109.05467](https://arxiv.org/abs/2109.05467).
- [95] J. Sinova, S. O. Valenzuela, J. Wunderlich, C. H. Back, and T. Jungwirth, *Rev. Mod. Phys.* **87**, 1213 (2015).
- [96] K. Samokhin, *Ann. Phys.* **324**, 2385 (2009).
- [97] G. H. Fecher, J. Kübler, and C. Felser, *Materials* **15**, 5812 (2022).
- [98] M. J. Park, S. Cheon, and H.-W. Lee, *Phys. Rev. B* **106**, 075140 (2022).